

# 3D Assembly of MXene Networks using a Ceramic Backbone with Controlled Porosity

Mert Arslanoglu, Bin Yuan, Rahul Panat,\* and O. Burak Ozdoganlar\*

Transition metal carbides (MXenes) are novel 2D nanomaterials with exceptional properties, promising significant impact in applications such as energy storage, catalysis, and energy conversion. A major barrier preventing the widespread use of MXenes is the lack of methods for assembling MXene in 3D space without significant restacking, which degrades their performance. Here, this challenge is successfully overcome by introducing a novel material system: a 3D network of MXene formed on a porous ceramic backbone. The backbone dictates the network's 3D architecture while providing mechanical strength, gas/liquid permeability, and other beneficial properties. Freeze casting is used to fabricate a silica backbone with open pores and controlled porosity. Next, capillary flow is used to infiltrate MXene into the backbone from a dispersion. The system is then dried to conformally coat the pore walls with MXene, creating an interconnected 3D-MXene network. The fabrication approach is reproducible, and the MXene-infiltrated porous silica (MX-PS) system is highly conductive (e.g.,  $340 \text{ S m}^{-1}$ ). The electrical conductivity of MX-PS is controlled by the porosity distribution, MXene concentration, and the number of infiltration cycles. Sandwich-type supercapacitors with MX-PS electrodes are shown to produce excellent areal capacitance ( $7.24 \text{ F cm}^{-2}$ ) and energy density ( $0.32 \text{ mWh cm}^{-2}$ ) with only 6% added MXene mass. This approach of creating 3D architectures of 2D nanomaterials will significantly impact many engineering applications.

## 1. Introduction

Transition metal carbides, generally referred to as MXenes,<sup>[1]</sup> are an emerging class of 2D nanomaterials that can bring exciting advances to a range of applications, such as energy storage,<sup>[2]</sup> catalysis,<sup>[3]</sup> water purification,<sup>[4]</sup> and sensing.<sup>[5]</sup> Their advantages include ultrahigh surface-to-volume ratio, tunable surface chemistry, outstanding mechanical strength, and unique optical, electrical, and catalytic properties.<sup>[6]</sup> Specifically, MXenes show superior electrochemical stability and high specific capacitance—exceeding many carbonaceous materials—making them promising candidates as supercapacitors.<sup>[2,7–9]</sup>  $\text{Ti}_3\text{C}_2\text{T}_x$  is a type of MXene produced by selective etching of Al atoms from the  $\text{Ti}_3\text{AlC}_2$  MAX phase.  $\text{Ti}_3\text{C}_2\text{T}_x$  has attracted much attention, primarily due to its well-established preparation process and its dispersibility in aqueous media without surfactants, owing to the presence of surface functional groups.<sup>[10]</sup> Several studies with  $\text{Ti}_3\text{C}_2\text{T}_x$  have demonstrated its significant potential for various


applications, including energy storage,<sup>[11–13]</sup> solar energy conversion,<sup>[14]</sup> and electromagnetic interference shielding.<sup>[15]</sup>

The use of MXene (or other 2D materials) in many device applications requires that a sufficient amount of material is available for electrochemical activities (e.g., intercalation in lithium-ion batteries). However, obtaining a large volume of 2D materials in 3D space poses a significant barrier. This is because MXenes and other 2D materials have a strong tendency to restack during assembly due to strong van der Waals forces. Restacking compromises the accessibility of individual flakes, greatly impeding their performance in surface-sensitive applications, such as electrochemical energy storage.<sup>[12,16,17]</sup> For instance, restacking impedes electrolyte penetration and ion diffusion in energy storage applications. The MXene layers located toward the center of the stack have a significantly reduced impact on the overall performance. This has been a critical problem in realizing practical applications of MXene, such as MXene-based electrochemical supercapacitors<sup>[12,13,16]</sup> that require interconnected 3D arrangements of 2D MXene nanoflakes to achieve the desired performance.

M. Arslanoglu, B. Yuan, R. Panat, O. B. Ozdoganlar  
Department of Mechanical Engineering  
Carnegie Mellon University  
Pittsburgh, PA 15213, USA  
E-mail: rpanat@andrew.cmu.edu; ozdoganlar@cmu.edu

R. Panat, O. B. Ozdoganlar  
Department of Materials Science and Engineering  
Carnegie Mellon University  
Pittsburgh, PA 15213, USA

R. Panat, O. B. Ozdoganlar  
Department of Biomedical Engineering  
Carnegie Mellon University  
Pittsburgh, PA 15213, USA

 The ORCID identification number(s) for the author(s) of this article can be found under <https://doi.org/10.1002/adma.202304757>

© 2023 The Authors. Advanced Materials published by Wiley-VCH GmbH. This is an open access article under the terms of the Creative Commons Attribution-NonCommercial License, which permits use, distribution and reproduction in any medium, provided the original work is properly cited and is not used for commercial purposes.

DOI: 10.1002/adma.202304757

The literature has reported several techniques for assembling MXene and other 2D nanomaterials<sup>[17,18]</sup> into 3D architectures.<sup>[19]</sup> These techniques may be categorized as direct fabrication methods and methods that use a (generally sacrificial) support structure. Several direct fabrication approaches involving freeze-drying and 3D printing have been reported specifically for the 3D arrangement of MXenes. MXene has also been combined with carbon network for Li–S battery applications.<sup>[20]</sup> In this work, however, the strength improvement achieved via this approach was not quantified. Levitt et al.<sup>[21]</sup> integrated MXene flakes into nanoyarns via bath electrospinning. Researchers used gelation to obtain freestanding 3D MXene aerogels by introducing chemical additives, such as Na<sup>+</sup> ions,<sup>[22]</sup> sodium alginate,<sup>[23]</sup> and ethylenediamine.<sup>[24]</sup> Several works used 3D printing to create MXene structures: Yang et al.,<sup>[25]</sup> and Orangi et al.<sup>[13]</sup> fabricated 3D MXene structures using extrusion-based printing of concentrated inks. Yang et al.<sup>[22]</sup> used sacrificial 3D-printed hollow (resin) templates with complex geometries, which were subsequently filled with MXene inks to achieve enhanced design customization. However, these fragile MXene aerogels required additional mechanical support without blocking the accessibility of the porous structure. Tetik et al.<sup>[12]</sup> combined inkjet-based 3D printing with ice templates to fabricate 3D MXene aerogels with complex geometries. As an alternative to aerogel-based 3D construction of MXene, researchers assembled 2D MXene nanosheets separated by 1D nanomaterials, e.g., MnO<sub>2</sub> nanowires,<sup>[26]</sup> or polymers, e.g., PANI,<sup>[27]</sup> to create 3D MXene structures, where the separating elements were used to eliminate the restacking.

Three techniques that use support structures for assembling 2D nanomaterials into 3D architectures have been described in the literature: direct drop casting, electrophoretic deposition, and chemical vapor deposition. Direct drop casting is used to create electrically conductive MXene-infiltrated textiles<sup>[28]</sup> and graphene-coated elastomeric foams.<sup>[29]</sup> However, nanomaterial agglomeration, limited infiltration depth, and the inherent challenge of achieving high loading amounts hinder the feasibility of this approach for many applications. Pan et al.<sup>[31]</sup> used electrophoretic deposition to fabricate MXene-coated carbon cloth as a flexible electrode material. Although electrophoretic deposition provides high precision, it requires electrically conductive porous scaffolds, limiting the types of materials used for the 3D support structure. Chemical vapor deposition has been used for the templated growth of graphene,<sup>[30]</sup> graphite,<sup>[32]</sup> and other 2D materials on scaffolds through the thermal decomposition of the precursor gases. However, the limited precursor availability restricts the range of materials deposited onto the porous scaffolds. Hence, the existing methods have yet to demonstrate the desired combination of versatility, reproducibility, and scalability of integrating various 2D materials into 3D support structures for practical applications, highlighting the need for further research in this field.

Several studies have shown the effectiveness of utilizing MXene-based electrodes in supercapacitor applications. The freeze-dried MXene aerogel-based electrodes presented by Wang et al.<sup>[23]</sup> and Li et al.<sup>[24]</sup> produced areal capacitances of 1.01 and 4.03 F cm<sup>-2</sup> with 15 and 14.2 mg cm<sup>-2</sup> active mass (MXene) loadings, respectively, at 2 mV s<sup>-1</sup> scan rate. The extrusion-based 3D printed MXene electrodes<sup>[13]</sup> produced an areal capacitance of 1.04 F cm<sup>-2</sup> (at 2 mV s<sup>-1</sup>) with 9.92 mg cm<sup>-2</sup> mass loading.

The MXene aerogel electrodes presented in ref. [22] exhibited an areal capacitance as high as 7.5 F cm<sup>-2</sup> (at 0.5 mA cm<sup>-2</sup>) with a mass loading of 54.1 mg cm<sup>-2</sup>. The electrodes that are formed by 2D MXene nanosheets separated by MnO<sub>2</sub> nanowires<sup>[26]</sup> and PANI<sup>[27]</sup> produced areal capacitances of 0.2 F cm<sup>-2</sup> (at 0.2 mV s<sup>-1</sup>) and 7.96 F cm<sup>-2</sup> (at 2 mV s<sup>-1</sup>) for MXene loadings of 1 and 23.61 mg cm<sup>-2</sup>, respectively. The flexible electrodes of MXene-integrated carbon cloth<sup>[31]</sup> revealed an areal capacitance of 5.73 F cm<sup>-2</sup> (at 5 mA cm<sup>-2</sup>) using 34.9 mg cm<sup>-2</sup> mass loadings. Although higher areal capacitances are reported in some of these works, achieving those required the use of higher amounts of active mass (MXene) loading, indicating that the capacitance achieved per unit MXene mass may be a more appropriate metric to describe the performance of MXene-based electrodes. By improving the 3D construction of 2D MXene, the performance of MXene-based electrodes and supercapacitors can be significantly increased using less active mass loading.

We have developed an entirely new material system comprising a 3D network of 2D MXene inside a porous ceramic backbone. We control the architecture of the 3D MXene network by adjusting the backbone's porosity distribution and the MXene infiltration into it. To achieve this, we utilize ceramic freeze casting to create porous silica structures that have open hierarchical porosity and a controlled porosity distribution. MXene is then infiltrated into the porous silica using capillary flow, and the system is dried out to create the MXene-infiltrated porous silica (MX-PS) system. The drying process enables the 2D MXene flakes to conformally coat the inner surfaces of the interconnected micropore network within the silica. The porous silica backbone thus facilitates the 3D assembly of MXene and offers essential attributes needed for electrochemical applications, such as mechanical strength, electrical insulation, and permeability. Importantly, the fabrication approach is reproducible and scalable. First, we report the reproducible fabrication of the MX-PS system and analyze the effects of porosity, MXene concentration, and infiltration cycles on conductivity. Next, we examine the directionality of electrical conductivity of the MX-PS samples arising from the selective orientation of the pores. We then demonstrate the effectiveness of MX-PS as electrodes on a sandwich-type supercapacitor, comparing their energy density and power capacity to the state-of-the-art MXene devices. To the best of our knowledge, this is the first work to create a controllable 3D MXene network architecture combined with a porous ceramic backbone.

## 2. Results and Discussion

The fabrication of MX-PS is summarized in **Figure 1**. We first fabricated porous silica backbones using unidirectional freeze casting of a camphene-based slurry, following the approach outlined in our previous work.<sup>[33]</sup> This freeze-casting approach produces porous silica backbones with open pores and directional porosity, including a major pore direction with increased pore connectivity and elongated pores, see Figure 1a; and Figure S1 (Supporting Information).<sup>[34,35]</sup> In this process, a ceramic or metal slurry is “frozen” anisotropically to create green porous structures with controlled porosity that are then sintered to achieve part strength. Freeze casting is a simple, scalable, and material-agnostic technique to develop open, controlled, hierarchical, and directional porosity. In our recent work, well-defined,

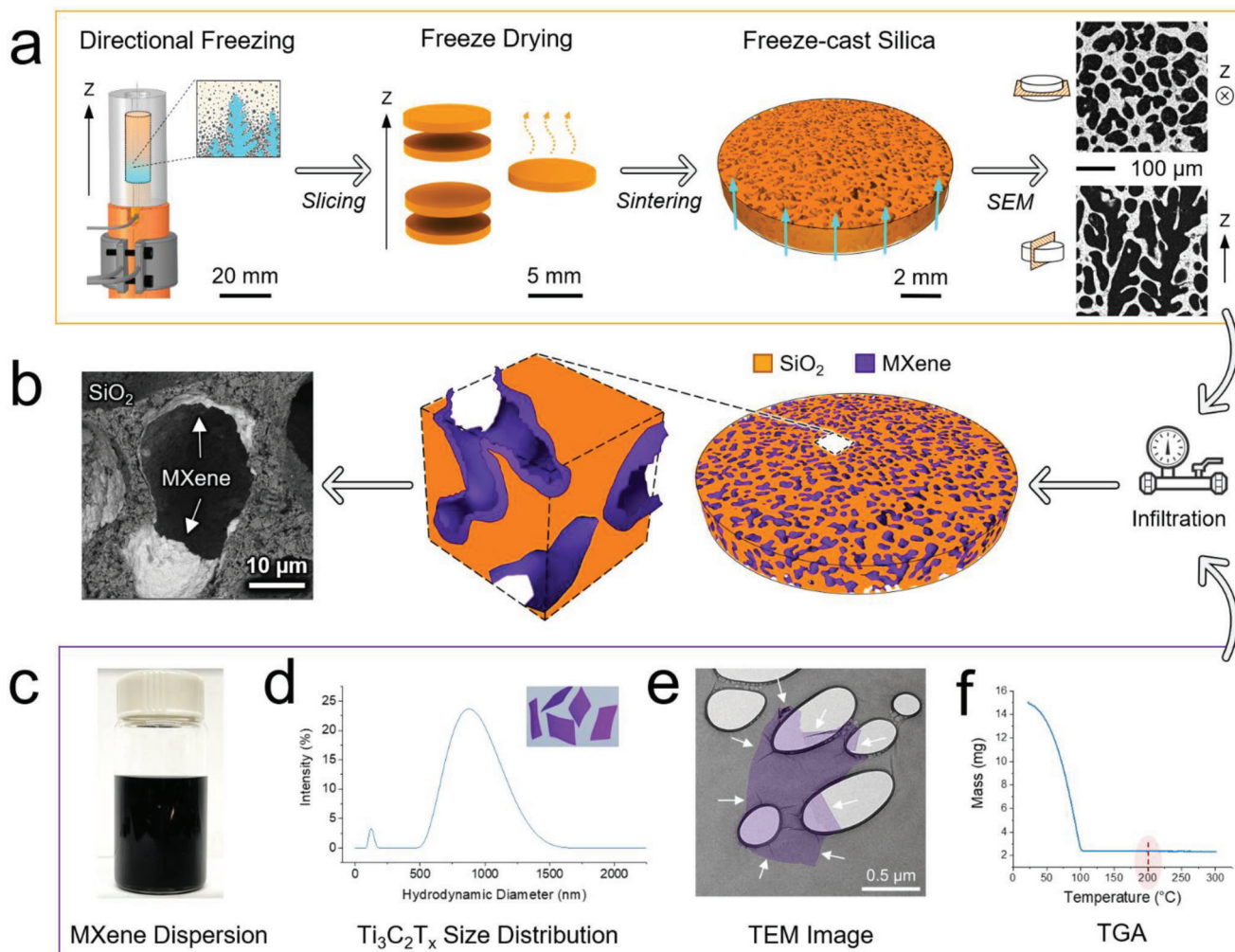


**Figure 1.** Fabrication of electrically conductive porous silica via infiltration of 2D MXene nanosheets. a) Preparation of silica discs with unidirectional porosity via freeze casting. The blue arrows represent the solidification direction and the main pore orientation. The SEM images show the horizontal (top) and vertical (bottom) cross-sections of the fabricated porous samples (scale bar = 100  $\mu\text{m}$ ). b) A MXene infiltrated porous silica sample with a zoomed-in 3D figure showing the thin-layer coating of internal pore surfaces by MXene flakes while preserving the structural porosity. A high-magnification back-scattered SEM image of an infiltrated sample shows the thin-layer MXene coating (scale bar = 10  $\mu\text{m}$ ). c) MXene dispersion prepared using the minimally intensive layer delamination (MILD) method.<sup>[8]</sup> d) The hydrodynamic diameter distribution of 2D  $\text{Ti}_3\text{C}_2\text{T}_x$  nanosheets for the prepared MXene dispersion. A solid model of the dispersed 2D flakes is given in the inset. e) TEM image showing the structure and the size of a single-layer  $\text{Ti}_3\text{C}_2\text{T}_x$  nanosheet with arrows indicating its periphery. False coloring (purple) is used to help with visualization. f) Thermogravimetric analysis (TGA) results for the remaining mass of MXene dispersion as a function of temperature. The mass value at 200  $^\circ\text{C}$  is used for calculating the MXene concentration of dispersions.

interconnected, and steerable internal porosity was achieved in silica via freeze casting.<sup>[33]</sup> Table S1 (Supporting Information) provides the specific pore volume, specific surface area, permeability, and pore tortuosity of the freeze-cast silica in this work, all of which were measured by mercury porosimetry. In parallel,  $\text{Ti}_3\text{C}_2\text{T}_x$  MXene of known hydrodynamic diameter was synthesized using the procedure described elsewhere.<sup>[10]</sup> The MXene is dispersed in deionized (DI) water at specific ratios to obtain MXene dispersions at desired concentrations, as shown in Figure 1c–e. The porous silica backbones were subsequently submerged in a dispersion of MXene to facilitate the infiltration of MXene into the pores of the backbone. Following the infiltration process, the samples were dried in a vacuum environment. This approach ef-

fectively facilitated capillary-driven conformal coating of the MXene onto the pore surfaces. Figure 1b shows a sample backbone with MXene coating the pore surfaces. The open porosity of the backbones enables the creation of MX-PS composite materials with the connected 3D assembly of MXene nanoflakes.

The morphology of the pores created on the porous silica backbone is critical to the architecture of the 3D MXene network. In this work, we followed the preparation steps outlined in our previous work<sup>[33]</sup> with 20% solid loading, 400 nm particle size, and  $-5$   $^\circ\text{C}$  freezing (bottom surface) temperature to fabricate porous-silica backbones. The resulting porous silica backbones exhibit  $\approx 60\%$  porosity with  $\approx 50$   $\mu\text{m}$  average pore size. The resulting pores can be observed from the cross-sectional images in

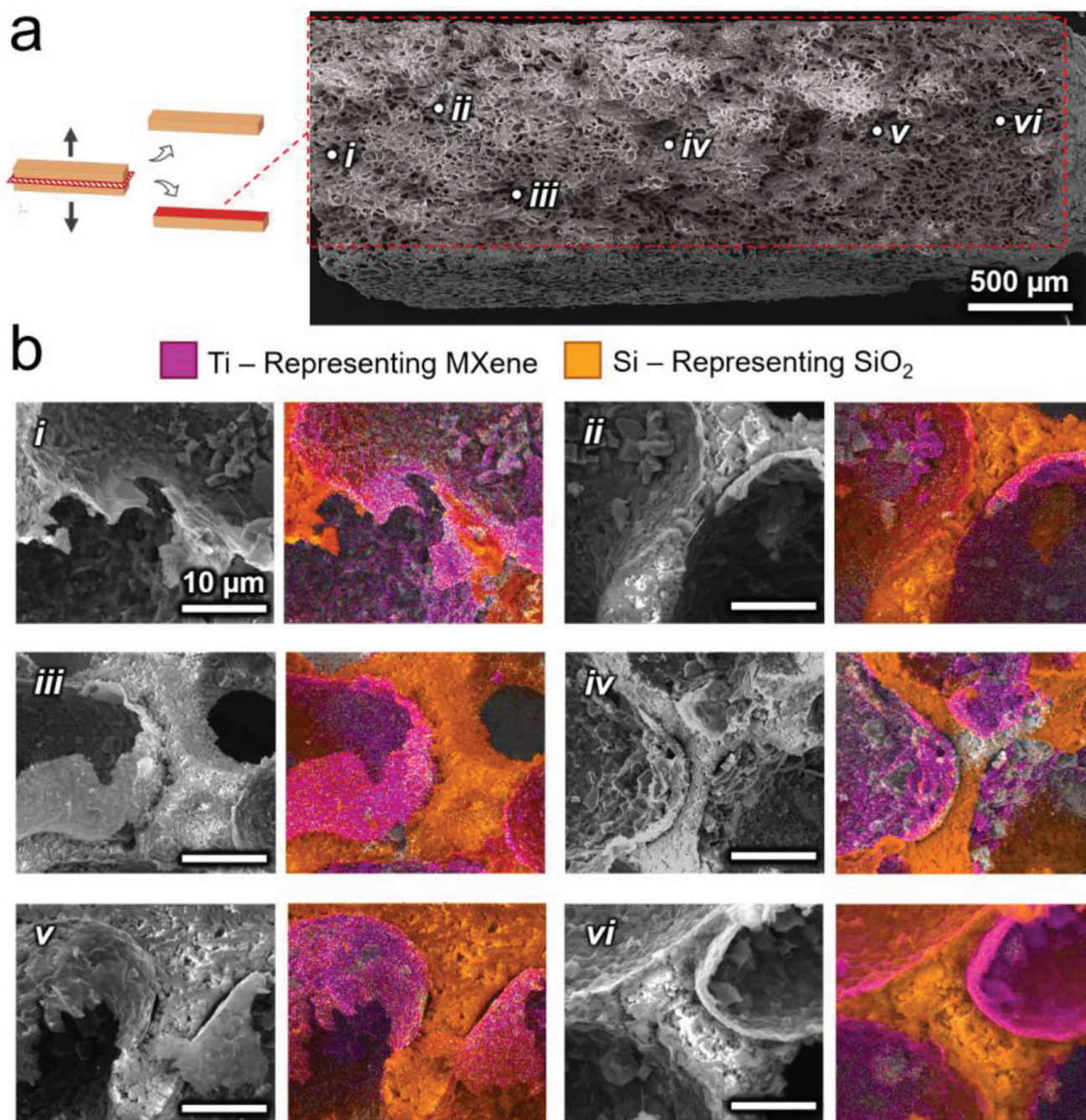


**Figure 2.** Experimental verification of the MXene infiltration process. a) An SEM image of a longitudinal cross-section of a rectangular sample used in the electrical conductivity measurements. The area labeled by the red-dashed rectangle indicates the boundaries of the analyzed cross-section. The schematic on the left illustrates the cross-sectioning process. b) Pairs of SEM images and EDX maps at the locations denoted in (a), confirming that MXene films exhibit a thin conformal morphology along the pore surfaces and the pore access is not blocked. In EDX maps, the purple color represents Ti (i.e.,  $\text{Ti}_3\text{C}_2\text{T}_x$  MXene) and the orange color is linked to Si (i.e.,  $\text{SiO}_2$ ). Scale bars in (a) and (b): 500  $\mu\text{m}$  and 10  $\mu\text{m}$ , respectively.

Figure 2a; and Figures S1a, S1b, and S2a (Supporting Information). The distributions for the equivalent pore diameter in the horizontal cross-sections, the maximum Feret diameter in the vertical cross-sections, and the pore orientation are presented in Figure S1c,d (Supporting Information), respectively. The ratio of open porosity of porous silica samples is estimated to be above

99.5% using Archimedes' method. A detailed statistical analysis of the pore characteristics due to the freeze casting of the silica-camphene material system is presented in our previous work.<sup>[33]</sup>

Freeze casting utilizes highly anisotropic solidification characteristics of a liquid (solvent) to template a hierarchical porosity,<sup>[33,34]</sup> as illustrated by the scanning electron microscopy

(SEM) images in Figure 1a; and Figure S1 (Supporting Information). The overall porosity and average pore size are primarily controlled by the solid loading of the initial slurry, whereas the pore morphology is determined by the material system, primarily by the solvent. For the same solid-loading level, the dendritic porosity created by camphene-based slurries results in a higher geometric surface area than the lamellar porosity created by water-based slurries.<sup>[36]</sup> For this reason, we chose camphene as the solvent in this work. The primary orientation of the templated porosity is dictated by the thermal boundary conditions applied during solidification. In camphene-based systems with unidirectional freezing (i.e., using a low-temperature system on one side), the freezing process forms highly elongated dendrites oriented normal to the freeze front. Perpendicular side branching of dendrites enables the formation of a 3D network comprising internally connected channels.

The capillary coating of MXene onto surfaces of pores inside the silica backbones is accomplished by infiltrating aqueous  $\text{Ti}_3\text{C}_2\text{T}_x$  MXene dispersions and vacuum-assisted drying. The single- and multilayer MXene nanosheets were suspended in the aqueous dispersions by an equilibrium of electrostatic, van der Waals, and hydrodynamic forces.<sup>[37,38]</sup> The backbones were then submerged into the MXene dispersions and refrigerated in sealed vials for 12 h to enable dispersion to penetrate the porous backbones fully through capillary flow and diffusion. The purpose of refrigeration is to minimize the oxidation of MXene during the process.<sup>[39]</sup> The samples were dried and their external surfaces were cleaned of excess MXene using damp foam-tipped swabs (see the Experimental Section for details). Table S2 (Supporting Information) provides the effect of the MXene concentration in the dispersant and the number of infiltration cycles on the mass of elongated cuboid-shaped porous silica samples ( $\approx 1 \text{ mm} \times \approx 1 \text{ mm} \times \approx 10 \text{ mm}$ ) with 60% porosity at different steps of the infiltration and surface cleaning processes.

Cross-sections of MX-PS samples were analyzed using SEM and energy-dispersive X-ray spectroscopy (EDX), as shown in Figure 2; and Figure S2 (Supporting Information). The SEM images and EDX mapping show the pore surfaces coated with a thin layer of MXene nanosheets and no blocking of pore access by the MXene sheets. The typical dendritic pore morphology is unchanged during the infiltration, as shown in the longitudinal cross-section at the mid-plane of an MX-PS sample in Figure 2a. Higher-magnification SEM images, as given in Figure 2b, revealed the 3D structure of thin and continuous MXene coating (purple) conformal to the pore surfaces of silica (orange). The texture difference between the MXene nanosheets (smooth) and the sintered silica particles (rough) can be seen in the grayscale SEM images. The different elements in these regions are identified by X-ray mapping, and the microstructure of the MX-PS is further clarified with the help of the unique color labeling of EDX.

In this infiltration approach, the 2D  $\text{Ti}_3\text{C}_2\text{T}_x$  MXene nanosheets with a high aspect ratio are transported into the 3D pore network by the hydrodynamic flow, supported by the capillary effect. To ensure the successful infiltration of the porous backbone, we applied a gentle vacuum pressure for 10 min during the process. This step facilitates the removal of any potentially trapped air bubbles that could compromise the quality and uniformity of thin-layer MXene coating. Establish-

ing a well-connected MXene network requires comprehensive infiltration of the dispersion into the porous backbones.

During drying, the free surface of the infiltrant (i.e., the concave meniscus of MXene dispersion inside pores) progresses inwards along the pores as the water departs the backbone through evaporation. The details of the mass transfer during the drying of porous media can be found elsewhere in the literature.<sup>[40]</sup> The shape and motion of the meniscus within the pores are controlled by the balance between evaporation and hydrodynamic flow.<sup>[41]</sup> While the evaporation causes solid accumulation on the channel surface,<sup>[42]</sup> the hydrodynamic flow within the MXene dispersion homogenizes the MXene concentration around the free surface by compensating for the evaporated liquid.<sup>[41]</sup> During drying, the contact line, i.e., the triple interface between the liquid infiltrant, pore surface, and air, becomes pinned to the surface until the final evaporation stage.<sup>[43,44]</sup> Near the contact line, evaporation is faster due to the higher curvature of the meniscus.<sup>[45]</sup> The MXene dispersion flows internally toward the contact line to replenish this region. However, the higher evaporation rate near the contact line creates a thermal gradient that lowers the surface tension, resulting in Marangoni flow in the opposite direction toward the center.<sup>[41,44]</sup> Usually, the outward flow (from the center of the channel to the contact line) is more dominant for spherical particles. Through this flow, more particles are carried toward the contact line and an excessive accumulation near the contact line is observed, also known as the coffee-ring effect.<sup>[44]</sup> However, as shown by Yunker et al.,<sup>[43]</sup> the shape of particles can change the flow dynamics and particle deposition during drying. Primarily determined by the electrostatic forces, strong long-ranged interactions between 2D MXene nanomaterials in water weaken the outward flow,<sup>[46]</sup> which helps to mitigate the coffee-ring effect caused by excessive accumulation of particles near the contact line. Instead, a thin and uniform MXene film is obtained with unobstructed pore access upon drying.<sup>[41,47]</sup>

Upon completion of the drying process, the  $\text{Ti}_3\text{C}_2\text{T}_x$  MXene nanoflakes adhere to both the (silica) pore surfaces and neighboring MXene flakes,<sup>[48]</sup> enabling the formation of a stable and well-anchored MXene coating on the backbone. Note that well-adhered silica nanoparticles have also been grown on MXene flakes.<sup>[49]</sup> The average adhesion energy between a single layer of  $\text{Ti}_3\text{C}_2\text{T}_x$  MXene and the oxidized layer of a silicon wafer is reported as  $0.90 \text{ J m}^{-2}$  in the literature, as measured by direct atomic force microscopy.<sup>[50]</sup> Since our process involves heating the green silica samples to  $1200 \text{ }^\circ\text{C}$ , however, we expect the chemistry of the silica surface to be different compared to the silica,<sup>[50]</sup> thus having a different surface interaction with MXene. The mechanical interlocking between the MXene flakes and the surface, resulting from the surface roughness, could further promote this adhesion (Figure S3a, Supporting Information). In some instances, as seen in Figure S3b (Supporting Information), the MXene sheets adhered to the protruded silica particles, cantilevering out of the local surface. As observed in Figure 2; and Figures S2 and S3 (Supporting Information) (and confirmed by many SEM images we analyzed), however, a vast majority of the MXene flakes adhere conformally to the interior pore surfaces of the silica backbone. We note that capillary flow and diffusion limits during infiltration may create a depth-dependent variation in the conformal MXene thickness. Although direct and quantitative data on the uniformity of the MXene layer is challenging, we

believe that restacking of MXene nanosheets is minimized based on our electrical conductivity measurements, large internal surface area, and SEM images. We assess the MXene coverage via conductivity measurements discussed later in this section.

One potential concern about using an aqueous dispersion for MXene is oxidation. Increased oxidation triggered by the water phase of the mixture could considerably diminish MXene's electrical properties with time.<sup>[39]</sup> However, unagitated MXene dispersions have been reported to exhibit a decrease in oxidation rate at concentrations above a critical value due to steric shielding.<sup>[51]</sup> This arises from overlapping edges of adjacent nanosheets within the dispersion and creates a physical barrier (capping and steric shielding) that prevents water access to the edges of the MXene sheets, slowing down their oxidation, when the concentration of MXene dispersion is above the critical value. For our system (e.g., 1  $\mu\text{m}$  flake size, 1 nm flake thickness, and 3.7  $\text{g cm}^{-3}$   $\text{Ti}_3\text{C}_2\text{T}_x$  MXene density), ref. [51] gives the critical MXene concentration that minimizes oxidation of MXene in the dispersion as 7.8  $\text{mg mL}^{-1}$ . Since all prepared dispersions in our work have higher concentrations than this critical value and are used immediately upon synthesis, the oxidation of water-dispersed MXene was minimized.

Conformally attaching MXene sheets to the connected network of pores inside the silica backbone creates a 3D assembly of the 2D MXene nanosheets. Through the capillary coating process, the MXene utilization is enhanced as the dispersed 2D  $\text{Ti}_3\text{C}_2\text{T}_x$  nanosheets are coated on the internal pore surfaces of the backbone. Since the nanosheets are spread out over an expansive surface area provided by the hierarchically porous silica, the number of restacked nanosheets is minimized. Limiting restacking is critical for obtaining optimal electrical properties of MXene to enable important potential applications, such as energy storage systems.<sup>[16]</sup> Moreover, the MXene utilization can be further increased by manipulating layer-to-layer interactions within the dried thin film on the pore surfaces. In literature, adding nanoparticles (0D),<sup>[52]</sup> nanofibers (1D),<sup>[53]</sup> or 2D nanoflakes<sup>[8]</sup> as physical separators, or tailoring the functional groups on MXene surfaces chemically<sup>[54]</sup> have been reported to mitigate restacking within such confined spaces. However, the effects of these approaches have not been studied in this paper.

The fabrication parameters used for creating the MX-PS samples directly affect their electrical conductivity. The preparation of MX-PS samples consists of three steps: fabricating silica backbones with controlled porosity using the freeze casting process; synthesizing MXene and preparing the dispersion with the desired MXene concentration; and infiltrating the MXene dispersion into the backbones and drying. Within each step, multiple factors are used to tune the spatial distribution of the MXene network and, thus, the electrical conductivity of the final MX-PS parts. In this study, we evaluated the effects of the MXene concentration of the dispersions, the number of infiltration cycles, and the porosity and pore orientation of backbones on the conductivity of MX-PS samples. Furthermore, we analyzed the effect of the storage time (i.e., the time elapsed since the fabrication of MX-PS parts) on the electrical conductivity of the samples.

We first evaluated the effect of MXene concentration in the dispersion on the electrical conductivity of the MX-PS samples. In electronics applications, silica is used as an electrical insulator due to its low conductivity of  $\approx 5 \times 10^{-12}$   $\text{S cm}^{-1}$  at 300 K.<sup>[55]</sup> The thin-layer coating of the interconnected network of MXene

nanosheets on the internal pore surfaces of the silica backbones makes the MX-PS samples electrically conductive. To assess the effect of MXene concentration on electrical conductivity, in addition to the MXene dispersion with 180  $\text{mg mL}^{-1}$  concentration, dispersions with concentrations of 45, 90, and 135  $\text{mg mL}^{-1}$  were prepared.

As seen in **Figure 3a**; and **Figure S4a** (Supporting Information), the electrical conductivity of MX-PS samples was found to increase by more than 30 folds as the concentration of the MXene dispersion is increased from 45  $\text{mg mL}^{-1}$  (1 vol%) to 180  $\text{mg mL}^{-1}$  (4 vol%). Electrical conductivity as high as 100  $\text{S m}^{-1}$  is obtained for single infiltration of 180  $\text{mg mL}^{-1}$  MXene concentration. To assess the reproducibility, three samples were tested for each concentration level; we observed relatively low variability in the conductivity of samples prepared nominally under the same conditions, especially at higher concentration levels. The increase in conductivity with MXene concentration was nearly exponential up to 135  $\text{mg mL}^{-1}$ , but the rate of increase was lower at higher concentrations (from 135 to 180  $\text{mg mL}^{-1}$ ).

The increased conductivity obtained at a higher concentration MXene dispersions is an expected result: the infiltration with higher MXene concentrations makes a larger number of nanosheets available for establishing a better-connected network. In addition, the concentration gradient between the infiltrant bath and the center of the backbones increases with an increase in MXene concentration. Based on Fick's law of diffusion,<sup>[56]</sup> this increased gradient imposes a higher diffusion flux for MXene nanosheets to infiltrate the porous backbone. This facilitates faster and easier infiltration of MXene nanosheets into the substrate pores, resulting in a more uniform and well-connected network. These synergistic effects enhance the overall electrical conductivity of the resulting MX-PS composite.

At lower MXene concentrations, we observed an exponential increase in conductivity with increased concentration. The rate of increase in conductivity diminishes at higher MXene concentrations, as shown in **Figure 3a**. As described in the literature (e.g., Lux<sup>[57]</sup>), the conductivity improvement in percolation-based systems is expected to converge to a saturation limit. With further concentration increases, the probability of forming additional conductive paths decreases, and the improvement in conductivity becomes less significant. In addition, at higher concentrations, the viscosity of the MXene dispersion increases rapidly, limiting the ability of the dispersion to penetrate and uniformly coat the substrate. This results in a nonuniform infiltration of MXene within the substrate and a less connected conductive network, leading to a saturation limit in conductivity improvement with increased MXene concentration. The dispersions prepared in this work comprise exfoliated single-layer and delaminated multilayer  $\text{Ti}_3\text{C}_2\text{T}_x$  MXene flakes.<sup>[10]</sup> The viscosity of a multilayer MXene dispersion is reported as 0.350 Pa s at a shear rate of 0.01  $\text{s}^{-1}$  when the volume fraction is 0.027,<sup>[37]</sup> which is within the volumetric concentration range of 0.01–0.04 used in this study. The viscosity increases exponentially with MXene concentration,<sup>[37,58]</sup> limiting the infiltrant's mobility into porous silica. Hence, the preparation of MXene dispersions with concentrations higher than 180  $\text{mg mL}^{-1}$  to further increase the electrical conductivity becomes challenging due to the high viscosity of the dispersion.

One potential approach to increasing the electrical conductivity of the MX-PS samples is to circumvent the high-viscosity

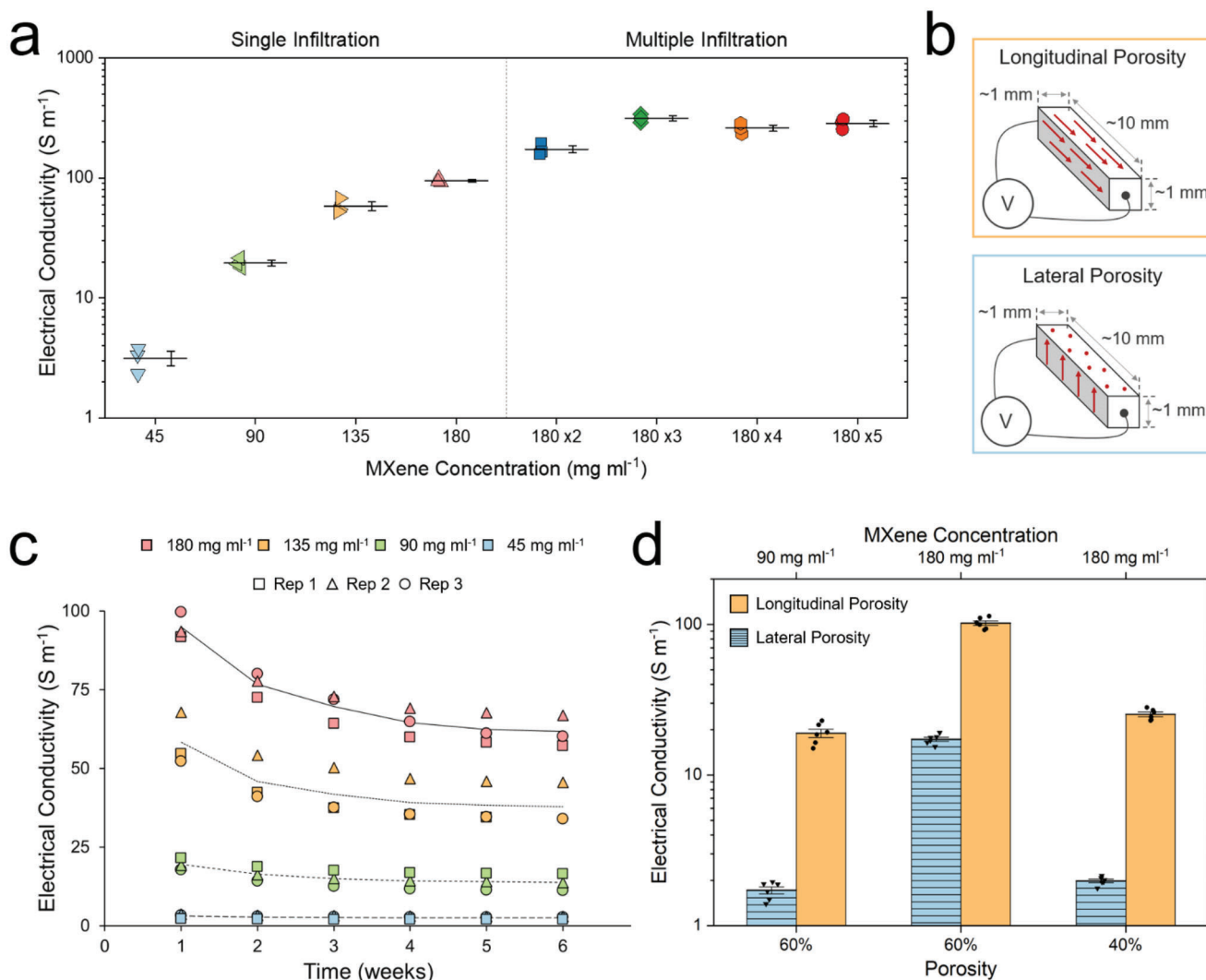


**Figure 3.** Electrical conductivity results of MXene infiltrated porous silica (MX-PS). a) Effects of the MXene concentration and the number of infiltration cycles on electrical conductivity of MX-PS samples (Left: single infiltration experiments, dispersions with MXene concentration of 45, 90, 135, and 180  $mg\ mL^{-1}$ ; Right: multiple infiltration with 180  $mg\ mL^{-1}$  MXene). b) Schematics showing the pore orientations of backbone: top—longitudinal porosity, as denoted by red arrows, aligned with the direction of electrical measurements; bottom—lateral porosity, as denoted by red arrows, perpendicular to the direction of electrical measurements. c) The effect of storage time on electrical conductivity for four separate MXene concentration levels: red—180  $mg\ mL^{-1}$ , orange—135  $mg\ mL^{-1}$ , green—90  $mg\ mL^{-1}$ , blue—45  $mg\ mL^{-1}$ . In (a) and (c), the results of three repetitions are reported for each data point. d) Electrical conductivity as a function of pore orientation: orange—longitudinal pore orientation; blue—lateral pore orientation.

limitation by using multiple infiltrations. To evaluate this approach, we infiltrated the backbones multiple times using the MXene concentrations of 180 and 90  $mg\ mL^{-1}$ . For each case, we tested three samples. As illustrated in Figure 3a; and Figure S4b (Supporting Information), when we used the dispersion with 180  $mg\ mL^{-1}$  MXene concentration, the conductivity increased more than three folds, reaching 340  $S\ m^{-1}$  in three infiltration cycles. However, subsequent infiltration cycles did not increase the conductivity further; indeed, a slight decrease in conductivity was observed. For a MXene dispersion at 90  $mg\ mL^{-1}$ , we observed an increase in conductivity from 18 to 51  $S\ m^{-1}$  after nine infiltration cycles as shown in Figure S4c (Supporting Information). The rate of increase and the final value obtained when the conductivity converged to its maximum were

both significantly lower for 90  $mg\ mL^{-1}$  as compared to those for 180  $mg\ mL^{-1}$ .

The increased conductivity with multiple infiltrations could arise from two mechanisms: higher network connectivity obtained by coating the uncoated surfaces with MXene and stacking an increased number of MXene layers on already coated surfaces. Both mechanisms likely play a role in the increased conductivity we observed. The “saturation limit,” i.e., the limitations to increasing the conductivity beyond a certain level, could also be explained by several mechanisms. First, the water content of MXene dispersion brings hydroxyl groups that accelerate the oxidation of the previously coated layer,<sup>[51]</sup> thereby reducing the conductivity. Second, once the percolation threshold is established, the quality of the network cannot be improved further.<sup>[57]</sup> Third,

the subsequent infiltration cycles could detach some of the previously deposited MXene layers. Fourth, the increased thickness of MXene layers may obstruct some of the smaller pores, limiting the penetration of further MXene. However, considering the low thickness of MXene layers and our SEM observations, we do not expect pore obstruction to affect subsequent infiltrations. And fifth, smaller pores can lead to diminished local capillary mobility due to reduced Reynolds number for the fluid flow,<sup>[59]</sup> preventing local wetting. The limited utilization of the backbone's porosity and surface area due to high viscosity may lower the saturation limit.

We further assessed the infiltration depth of MXene into the porous silica backbone relevant to the length scale of the current work. We infiltrated cube-shaped MX-PS samples with an edge length of  $\approx 10$  mm, which is roughly ten times larger than the thickness of our MX-PS electrodes we used in our demonstrative applications (see below). We applied both single and multiple (five) infiltration cycles to also capture the effect of infiltration cycles on MXene concentration with depth. Figure S5a,b (Supporting Information) shows the SEM images of the single-infiltration case, where a section at the center ( $\approx 5$  mm inside) of the sample is indicated. The major pore direction (and, thus, the main infiltration direction) is indicated by the arrows on the images. Figure S5c (Supporting Information) shows the associated EDX analysis of the indicated section, where the detected Ti shows the presence of MXene. Figure S5d–f (Supporting Information) provides the corresponding images for the sample with five times MXene infiltration. Again, we can detect Ti (and, thus, MXene) 5 mm inside the sample. Furthermore, we include a video showing the porous silica backbone at the beginning of the infiltration process (Movie S1, Supporting Information). Note also that larger samples may require longer infiltration durations. Based on the observations from this study, we conclude that MXene can penetrate porous silica samples at least to a depth of 5 mm for both the single- and multiple-infiltration cases.

An important question is whether the conductivity of the MX-PS samples changes with the storage time. To address this question, the conductivity of the MX-PS samples was measured weekly for 6 weeks. For each case, we tested 3 samples. During this time, the samples were stored under low pressure (120 mbar) at 4 °C except when measuring the resistance. As seen in Figure 3c, the conductivity exhibited some decay with time. By Week 6, the electrical conductivity of MX-PS samples decreased and converged to  $\approx 70\%$  of their respective initial value. We also measured the decay in the conductivity of the MXene aerogel (the synthesis of which is described in the Experimental Section) molded in a prismatic shape with 1 mm  $\times$  1 mm  $\times$  10 mm dimensions, where the conductivity was measured along the long direction. As shown in Figure S6 (Supporting Information), compared to the reduction in conductivity of the MX-PS samples, about three times faster degradation is observed for the MXene aerogel after one week ( $\approx 60\%$  reduction in conductivity for MXene aerogel vs 20% for MX-PS samples).

The likely reason for the observed reduction in conductivity is the oxidation of MXene sheets. The 2D MXene nanosheets on pore surfaces are prone to oxidation due to the available hydroxyl anions in the environment.<sup>[51]</sup> These anions interact with the MXene nanosheets through the voids between the flake layers inside the thin surface coating<sup>[60]</sup> and the carbon vacancies

within flakes originating from the source material.<sup>[61]</sup> The oxidation stability can be improved by controlling the temperature and exposure to oxygen or water molecules.<sup>[62]</sup> Although our samples were stored under low pressures, there is still a considerable number of oxygen molecules at these vacuum levels, which could cause the oxidation of MXene sheets. Sealing the outer surfaces of the MX-PS samples or filling the samples with a tertiary material (e.g., an elastomer) could minimize oxidation.

The electrical conductivity of MX-PS samples also depends on the porosity and pore-size distribution of the backbone since the amount and network connectivity of MXene are a direct function of the internal area and pore connectivity. The 3D surface interactions between the silica surface and the 2D nanosheets that conform to the internal pore walls provide the structural stability of the conductive MXene network within the samples. Therefore, controlling the porosity of the backbones is critical for successful infiltrations of MXene, and hence, higher electrical conductivity. To evaluate the effect of the backbone's porosity on the conductivity of the MX-PS samples, we tested backbones with 40% and 60% porosity, obtained by using silica solid loading of 40% and 20% during freeze casting, respectively. For each case, we tested 6 samples. As seen in Figure 3d, for 180 mg mL<sup>-1</sup> MXene concentration, reducing the porosity from 60% to 40% caused approximately a fivefold reduction in the conductivity of the MX-PS samples.

This substantial decrease in conductivity arises primarily from the reduced internal surface area of the lower-porosity backbones. The increased solid loading also results in smaller pore sizes and narrows the pore size distribution. Increasing the silica solid loading from 20% to 40% decreases the average pore size in the backbone from  $\approx 50$  to  $\approx 20$   $\mu\text{m}$ .<sup>[33]</sup> Considering the viscosity of the MXene dispersions and the size of MXene nanosheets, the reduction in pore size can reduce the infiltration efficiency. The capillary action can draw water into smaller pores while leaving the MXene nanosheet behind, creating a phase separation. These findings highlight the ability to modulate the MX-PS properties (here conductivity) via optimizing process parameters such as solid loading to obtain desired material characteristics.

Considering how the MXene network forms within the backbones, we expect a significant dependence of electrical conductivity on pore orientation. The electrical conductivity of the MX-PS samples with different pore orientations was measured to characterize the effect of pore orientation. For this purpose, cuboid-shaped MX-PS samples with 10 mm length were prepared, and the resistance was measured along (longitudinal) and normal to (lateral) the primary pore orientation, see Figure 3b. We observed that the electrical conductivity for longitudinal pore orientation was approximately an order of magnitude higher than that for the lateral pore orientation. Furthermore, this significant effect of pore orientation was present at different MXene dispersion concentrations (90 and 180 mg mL<sup>-1</sup>) and different backbone porosities (40% and 60%).

Unidirectional freeze casting using a camphene-based solvent templates a dendritic and hierarchical porosity within the silica backbones. The primary dendrite growth direction determines the primary pore orientation; in unidirectional freezing, the primary dendrite direction (i.e., the “trunks” of the tree-like shapes) is aligned with the thermal gradient (i.e., perpendicular to the freeze front). This result can be explained by considering the



MXene network established within the freeze-cast backbones. Thus, we expect a more direct connection of the MXene network along the primary pore orientation. The internal surfaces of this anisotropic porosity provide the pathways for creating an aligned interconnected network of MXene, which is critical for obtaining high electrical conductivity.<sup>[60]</sup> Additional connections between the main channels are obtained by the side channels (formed by the side branching of camphene dendrites during solidification), strengthening the MXene network. To quantify the mechanical advantage provided by the freeze-cast silica to the infiltrated MXene, we carried out compression tests on the silica backbone samples (the testing procedure is provided in the Experimental Section). For comparison, we also fabricated freeze-dried MXene aerogels in our lab (see Experimental Section for the synthesis) and subjected them to compression under identical conditions. Figure S7 (Supporting Information) shows a representative engineering stress–strain plot for 60% nominally porous freeze-cast silica (compressed along the freezing direction) and the MXene aerogel (the experiment was repeated on at least four different samples, each producing similar results). The average compressive strength of the silica backbone was about 1.9 MPa, and the average compressive strength of the MXene aerogel was about 1 kPa. The strength enhancement by arranging MXene in the silica backbone is thus over 3 orders of magnitude. The elastic modulus of the porous silica backbone was about 50 MPa, while that for the MXene aerogel is about 6.5 kPa. Thus, a significant mechanical advantage is obtained via our approach of 3D arrangement of 2D MXene flakes using freeze-cast porous silica backbone.

The pore size, pore elongation, and side branching are all controlled by the initial solid loading and freezing direction, which are controllable freeze-casting parameters. The elongation and orientation of the pores are described by their Feret properties,<sup>[33]</sup> which describe the morphology of the interconnected porosity. Thus, the obtained anisotropic electrical conductivity is controlled by these morphological porosity parameters of the freeze-cast backbone. Therefore, we can obtain highly anisotropic or isotropic electrical conductivity in MX-PS samples by dictating the porosity distribution. We note that isotropic porosity can be obtained by establishing omnidirectional freezing, e.g., submerging the slurry into a cooling bath.<sup>[34]</sup>

To demonstrate the utilization of electrically conductive MX-PS samples in a case study, we constructed sandwich-type (or button-type) two-electrode supercapacitor assemblies<sup>[63]</sup> that use disk-shaped MX-PS free-standing electrodes in a symmetric arrangement, see **Figure 4a**. For this purpose, we used backbones with 60% porosity and infiltrated them with 180 mg mL<sup>-1</sup> MXene dispersions. To better illustrate the effect of MXene infiltration, we also constructed a capacitor with the same design using non-infiltrated silica backbones as electrodes; we refer to this supercapacitor as a “non-MXene supercapacitor.” To assess the electrochemical performance of the supercapacitors, we performed electrochemical impedance spectroscopy (EIS), cyclic voltammetry (CV), galvanostatic charge–discharge (GCD) tests, and calculated their capacitance (see the Experimental Section for details).

The results of CV at scan rates of 2, 5, 10, 20, 50, 100, and 200 mV s<sup>-1</sup> are given in **Figure 4b** for the supercapacitor with MX-PS electrodes. The responses in the positive and negative sweep regions of the CV curves are symmetric at every scan rate,

implying a reversible charge–discharge behavior. The maximum currents, recorded at the boundaries of the selected potential window, show a notable increase with scan rate while the overall shape of the curves remains unchanged. **Figure S8a** (Supporting Information) reveals the significant difference in CV curves for the MX-PS supercapacitor and non-MXene supercapacitor at a scan rate of 10 mV s<sup>-1</sup>.

Due to rapid Faradaic surface reactions, pseudocapacitive materials, such as MXene offer much higher capacitance and rate capability (i.e., an ability to charge and discharge at different current densities) than electric-double-layer capacitors (EDLC), which rely only on the capacitive charge storage at the electrode–electrolyte interface.<sup>[64]</sup> Therefore, the strong performance of MX-PS supercapacitors can be attributed to pseudocapacitance.<sup>[9,65]</sup> In addition, as schematically depicted in **Figure 4e**, the thin MXene coating on the internal walls of freeze-cast silica enables electrons from the current collector to travel freely and cover a larger surface area. Thus, the porous structure is better utilized, and the active zone is expanded, enhancing the mobility of anions/cations in the electrode material. The higher number of electrons on the porous electrode surface attracts more ions from the neighboring electrolyte, increasing the effective surface area and the electrochemical double-layer capacitance during fast charge–discharge processes.<sup>[66]</sup> Therefore, the electrochemical performance of the MX-PS supercapacitors is considerably better than that of the non-MXene supercapacitors.

The GCD measurements for the MX-PS supercapacitor are presented in **Figure 4c** at different current densities. A comparison of the GCD curves of the MX-PS supercapacitor and non-MXene supercapacitor is given in **Figure S8b** (Supporting Information) at a current density of 2 mA cm<sup>-2</sup>, highlighting the significantly enhanced performance of the MX-PS supercapacitor. The GCD curves of MX-PS supercapacitors show a quasi-triangular shape with a symmetric charge–discharge behavior. The MX-PS supercapacitor exhibits an almost linear discharging curve, indicating a consistent and predictable discharge behavior, likely associated with the pseudocapacitive behavior.<sup>[64]</sup> The discharge duration is remarkably long due to improved charge storage capacity and pseudocapacitance of Ti<sub>3</sub>C<sub>2</sub>T<sub>x</sub> MXene in acidic (H<sub>2</sub>SO<sub>4</sub>) electrolytes.<sup>[9,64]</sup> Also, the MX-PS supercapacitor has a minor voltage drop, referred to as the IR drop, in GCD curves at the beginning of the discharge cycle. The IR drop is related to the internal resistance of the supercapacitor, and a small IR drop indicates a low internal resistance of a supercapacitor,<sup>[67]</sup> desirable for efficient energy storage. These characteristics of MX-PS supercapacitors enable achieving high current densities of up to 30 mA.

The Nyquist plot showing the results of the EIS for the MX-PS supercapacitor is given in **Figure 4d**. The results in the high-frequency region of the Nyquist plot indicate that the MX-PS supercapacitor has good electrical conductivity; this indicates a low internal resistance, confirming the small IR drop observed in the GCD curves. The internal resistance of supercapacitors can be calculated by adding the resistances of the electrode, the electrolyte in the porous structure of the electrode, and the contact resistance between the electrode and the current collectors. The high metallic conductivity of MXene<sup>[60]</sup> and the well-connected MXene network on silica backbones lower the internal resistance

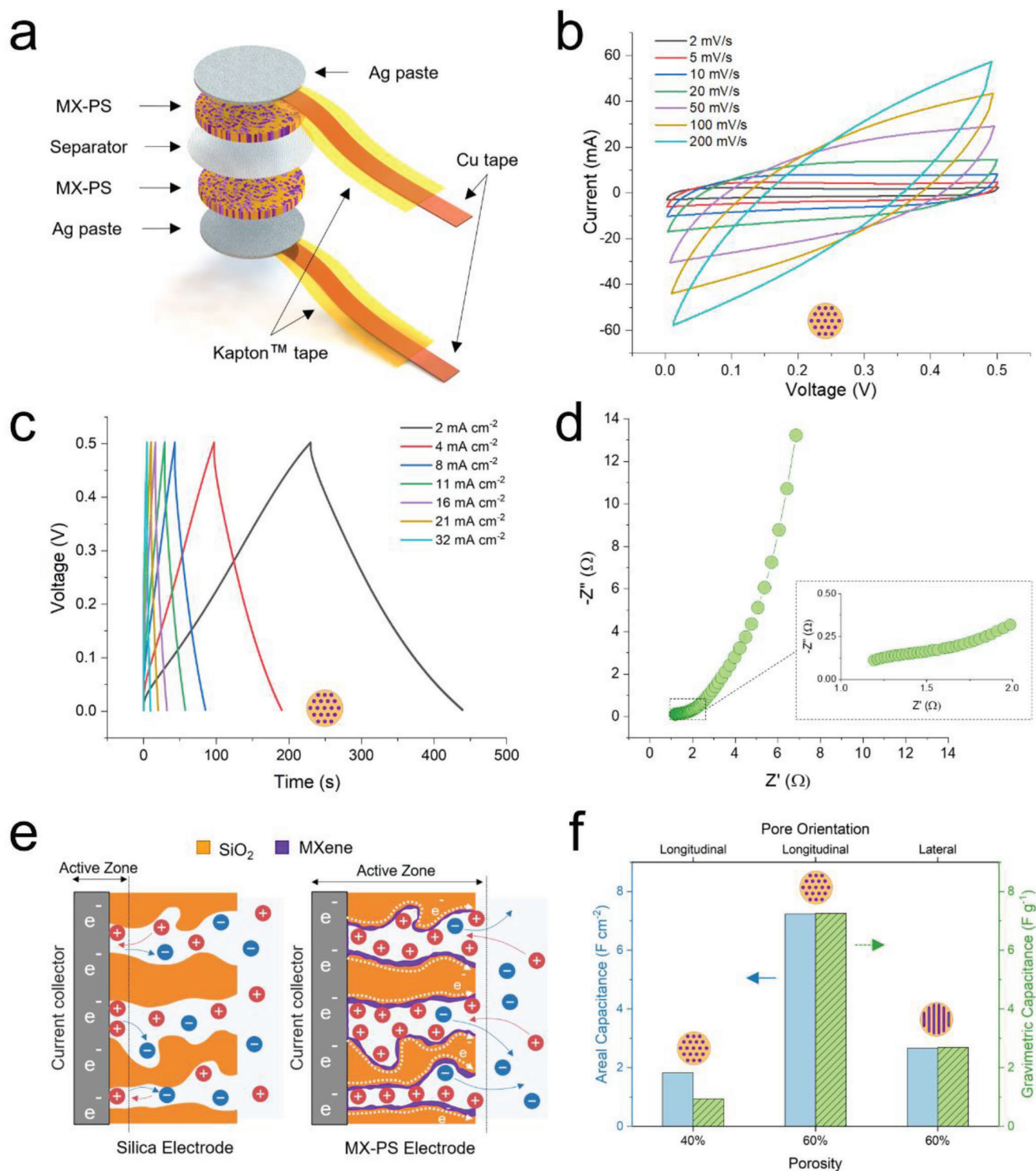


**Figure 4.** Supercapacitor results. a) Schematic of the sandwich-type supercapacitor structure. b) CV curves for the MX-PS supercapacitor at different scan rates. c) Galvanostatic charge–discharge curves for the MX-PS supercapacitor at different current densities. d) Nyquist plot (EIS) showing the impedance of the MX-PS supercapacitor. The inset gives a detailed view of the high-frequency range. e) Schematic illustration showing the increased active zone due to the presence of MXene on pore surfaces. f) Tunability of the areal (blue, left y-axis) and gravimetric (green, right y-axis) capacitance of the assembled supercapacitors by changing the porosity (bottom x-axis) and pore orientation (top x-axis) of freeze-cast silica backbones of the MX-PS electrodes. The circular sketches in each column represents the pore orientation from top-view of the electrodes: longitudinal pore orientation—out-of-plane pores; lateral pore orientation—in-plane pores.

significantly. A lower internal resistance reduces the energy loss via heat generation during charge–discharge cycles, enhancing the electrochemical performance. At the low-frequency range of the Nyquist plot, the MX-PS supercapacitor exhibits a steep slope, indicating an ideal capacitive behavior. The amplitudes of the impedances for MX-PS and non-MXene supercapacitors are plotted in Figure S8c (Supporting Information), revealing a dramatic difference between the two.

The areal and gravimetric capacitances of the MX-PS supercapacitor were calculated from the CV curves at a scan rate of  $10 \text{ mV s}^{-1}$  as  $7.24 \text{ F cm}^{-2}$  and  $7.26 \text{ F g}^{-1}$ , respectively. These results were obtained using infiltration with the MXene dispersion of  $180 \text{ mg mL}^{-1}$  concentration, resulting in an active (MXene) mass loading—MXene-to-backbone mass ratio—of 6%. The mass increase in porous silica due to MXene infiltration is given in Table S2 and Figure S9 (Supporting Information). Also, the effect of MXene concentration on the electrochemical performance is briefly evaluated by comparing these results with the ones of a supercapacitor prepared with a reduced MXene concentration of  $90 \text{ mg mL}^{-1}$ . The calculated areal capacitance for the MX-PS supercapacitor prepared with the MXene concentrations of  $90 \text{ mg mL}^{-1}$  is  $3.13 \text{ F cm}^{-2}$ , at the scan rate of  $10 \text{ mV s}^{-1}$ . The corresponding CV and GCD results are given in Figure S10 (Supporting Information). Overall, the electrochemical performance of the MX-PS supercapacitor can be tuned by changing the input parameters to the system such as the MXene concentration during infiltration.

We next evaluated the effect of porosity on the areal and gravimetric capacitances of the MX-PS supercapacitors, see Figure 4f. MX-PS electrodes from silica backbones with 40% and 60% (longitudinal) porosity were infiltrated with the MXene dispersion of  $180 \text{ mg mL}^{-1}$  concentration and were assembled into supercapacitors. The capacitance values were then calculated from the CV curves obtained at a scan rate of  $10 \text{ mV s}^{-1}$ . The capacitance was seen to increase four folds when using electrodes with 60% porosity than with 40% porosity. This significant effect can be explained by the increased average pore size and total pore volume of higher-porosity backbones, enhancing pore accessibility, and facilitating the infiltration of MXene nanosheets. Also, the difference in the gravimetric capacitances due to porosity is relatively larger than that in the areal capacitances. Lower porosity causes reduced MXene infiltration and increased total mass for the same projection area. The corresponding CV and GCD curves for the supercapacitor with the 40% porosity electrodes are given in Figure S11 (Supporting Information).

The effect of pore orientation of the MXene infiltrated electrodes on the electrical performance of the supercapacitors was investigated next using electrodes with 60% porosity. Electrodes with longitudinal and lateral pore orientations were used in separate supercapacitor assemblies. Although the total pore volume and the average pore size were the same for the electrodes, the electrodes with longitudinal porosity (i.e., pores mainly oriented toward the counter electrode) produced nearly three times higher capacitance than those with lateral porosity. This is an expected result considering the conformal MXene network that forms inside the porous samples. For electrodes with longitudinal porosity, the primary pore orientation toward the counter electrode creates a shorter (i.e., more direct) electrical pathway. Considering the anisotropy of pore geometry, the infiltrated MXene network

has better connectivity along the primary pore orientation than the side branches. However, for electrodes with lateral porosity, the electrical pathway is formed through the internal connections of the dendritic side branches, creating more tortuous pathways. Therefore, the resistance of the supercapacitor with lateral porosity is higher than that of the supercapacitor with longitudinal porosity. The Nyquist plots for the two cases are given in Figure S12 (Supporting Information), and the CV and GCD curves for the supercapacitor with lateral pore orientation are given in Figure S13 (Supporting Information).

Although design optimization and comprehensive analysis of supercapacitors are beyond the scope of this work, we wanted to demonstrate the cycle life stability of the MX-PS supercapacitors. For this purpose, we used MX-PS supercapacitors with longitudinal porosity and  $180 \text{ mg mL}^{-1}$  MXene concentration and ran up to 10 000 GCD cycles through repeated charge–discharge at  $32 \text{ mA cm}^{-2}$  current density, as illustrated in Figure S14 (Supporting Information). The capacitance retention of the MX-PS supercapacitor was 75.3%, after 10 000 cycles. This performance is within the range<sup>[68]</sup> or better than<sup>[69]</sup> that reported in the literature for MXene-based supercapacitors, but can be further improved. For example, the current density used in the cycling test was  $32 \text{ mA cm}^{-2}$ , whereas the lowest value we tested in the GCD experiments was  $2 \text{ mA cm}^{-2}$ , as shown in Figure 4c. Using a lower current density could further improve the cycling stability of supercapacitors by reducing the likelihood of damage or degradation to the electrode and electrolyte materials and minimizing heat generation. Carrying out tests in inert environments can also reduce oxidation-driven degradation. Additionally, the cyclic-charging results of supercapacitors could vary by the pH of the electrolyte (acidic vs neutral),<sup>[65]</sup> the size of the MXene nanosheets,<sup>[70]</sup> and the interlayer spacing of MXene.<sup>[53]</sup> For instance, MXene nanoparticles,<sup>[71]</sup> polyaniline nanofibers (PANINFs),<sup>[53]</sup> or cellulose nanofibrils (CNFs)<sup>[72]</sup> can be used to control the interlayer spacing while providing additional structural stability and minimizing the restacking of 2D MXene nanolayers. Incorporating these factors will be the subject of a future investigation. Additional discussion is given in Section S1 (Supporting Information).

We used the areal capacitance to evaluate the electrochemical performance of the MX-PS supercapacitors. Areal capacitance expresses the electrochemical performance of a supercapacitor for the projected device area; a high areal capacitance is preferred in electronic device applications.<sup>[73]</sup> Figure 5a,b presents the reported areal capacitances of MXene-based electrodes as a function of MXene mass loading from the literature, including supercapacitors based on 3D Na-MX,<sup>[22]</sup> MX/ $\text{WO}_x$ ,<sup>[31]</sup> MX/PANI,<sup>[27]</sup> MX/SA-5,<sup>[23]</sup> MX Aerogel,<sup>[24]</sup> 3DP MX,<sup>[25]</sup> Extruded MX,<sup>[13]</sup> MX/ $\text{MnO}_2$ ,<sup>[26]</sup> and MX Clay.<sup>[74]</sup> The MX-PS electrodes show excellent areal capacitance of  $7.24 \text{ F cm}^{-2}$  with  $\approx 2.4 \text{ mg cm}^{-2}$  of  $\text{Ti}_3\text{C}_2\text{T}_x$  MXene, indicating effective MXene utilization. Based on our infiltration approach, the dispersed MXene nanoflakes, which would otherwise form a dense restacked film, are diffused into the pores spreading out over the large surface area of the porous backbone. This process is expected to increase the area of the exposed individual MXene flakes for electrochemical reactions, enabling better utilization of MXene and improved performance of MX-PS supercapacitors from this work as shown in Figure 5a,b.

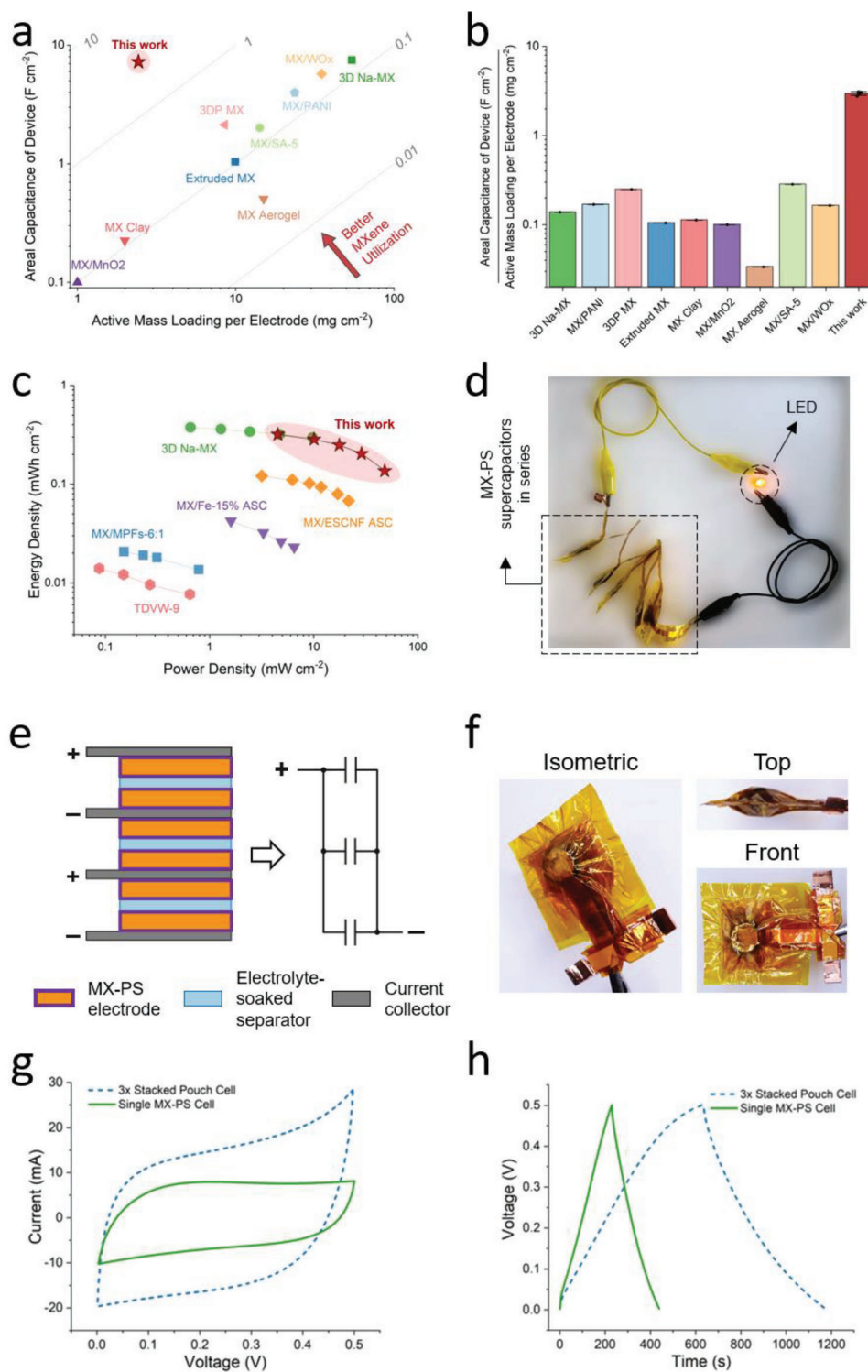


**Figure 5.** Comparison of our results with the literature and additional device configurations. a, b) Areal capacitance comparison of MX-PS supercapacitors with the values of previous MXene-based studies with various mass loadings of active materials from the literature (e.g., 3D Na-MX,<sup>[22]</sup> MX/WO<sub>x</sub>,<sup>[13]</sup> MX/PANI,<sup>[27]</sup> MX/SA-5,<sup>[23]</sup> MX Aerogel,<sup>[24]</sup> 3DP MX,<sup>[25]</sup> Extruded MX,<sup>[13]</sup> MX/MnO<sub>2</sub>,<sup>[26]</sup> and MX Clay.<sup>[74]</sup>). The diagonal dashed lines in (a) represent areal capacitance per active mass loading, i.e., utilization. c) Area-normalized Ragone plot comparing the energy density and power density of MX-PS supercapacitors (this work) with several sandwich-type supercapacitors from the literature (e.g., symmetric TDVW-9,<sup>[75]</sup> symmetric MX/MPFs-6:1,<sup>[76]</sup> asymmetric MX/Fe-15%/MnO<sub>2</sub>/CC,<sup>[77]</sup> asymmetric Ti3C2 MX Aerogel // ESCNF,<sup>[24]</sup> and symmetric 3D Na-MX.<sup>[22]</sup>). d) Optical photo of a yellow/orange LED powered by five serially connected MX-PS supercapacitors with longitudinal porosity. (MXene concentration = 180 mg mL<sup>-1</sup>). e) Schematic of the stacked cells fabricated for demonstration of scalability. f) Optical images of the stacked cells in the form of a pouch cell. g) CV curves of the single

We also calculated the MX-PS supercapacitors' areal energy density and areal power density. They produced an areal energy density of  $0.32 \text{ mWh cm}^{-2}$  and an areal power density of  $4.57 \text{ mW cm}^{-2}$  at a current density of  $2 \text{ mA cm}^{-2}$ . At an increased current density of  $32 \text{ mA cm}^{-2}$ , the power density increased to  $65.31 \text{ mW cm}^{-2}$ , while the energy density decreased to  $0.09 \text{ mWh cm}^{-2}$ . As shown in the area-normalized Ragone plot in Figure 5c, these values are higher than most of the previously reported values for MXene-based sandwich-type supercapacitors from the literature, including symmetric TDVW-9,<sup>[75]</sup> symmetric MX / MPFs-6:1,<sup>[76]</sup> asymmetric MX/Fe-15%/MnO<sub>2</sub>/CC,<sup>[77]</sup> asymmetric Ti<sub>3</sub>C<sub>2</sub> MX aerogel//ESCNF,<sup>[24]</sup> and symmetric 3D Na-MX.<sup>[22]</sup> As an overall demonstration, we connected five MX-PS supercapacitors serially after charging each up to 0.5 V and connected them to an LED light with an operating voltage of  $\approx 2.5 \text{ V}$ . The supercapacitors successfully powered the LED, as shown in Figure 5d.

To further demonstrate the scalability of our approach, we constructed a triple-stack pouch cell using our MX-PS electrodes and assessed its electrochemical performance. A schematic illustration of the pouch-cell assembly is shown in Figure 5e, and the optical images of the assembled pouch cell are given in Figure 5f. The pouch cell consists of six MX-PS samples used as two double-sided and two single-sided electrodes. The electrodes are separated by electrolyte-soaked porous polypropylene membranes. Figure 5g presents the CV curves of the single MX-PS supercapacitor and the stacked pouch cell at a scan rate of  $10 \text{ mV s}^{-1}$  in a potential window of 0–0.5 V. Similar to that for a single cell, a typical pseudorectangular shape is observed for the pouch cell. The area under the curve of the stacked pouch cell is considerably higher than that of the single cell, demonstrating that the stacked device contains more electroactive species and thus provides an extra charge for the storage mechanism. As can be seen in Figure 5h, the discharge duration increased by approximately threefold with the stacked configuration compared to the single cell, indicating a threefold increase in capacitance storage. Even though the pouch cell comprises a larger contact area due to multiple interfaces between the MX-PS electrodes and the separators, linear and symmetrical charge–discharge behavior is preserved with a negligible IR drop. Additionally, EIS was conducted to assess the resistivity of the pouch cell. As shown in the Nyquist plot depicted in Figure S15a (Supporting Information), a similar curve was obtained for the pouch cell with a low resistance value at the high-frequency region and a steep increase in the low-frequency region. The impedance of the pouch cell remained low comparable to that of the single cell over the entire frequency domain tested in EIS, as shown in Figure S15b (Supporting Information).

We note that the pore sizes of the silica backbone increase as a function of distance from the constant-temperature cooling surface (Figure 1a).<sup>[33]</sup> The sample-to-sample pore diameter variation for our MX-PS samples was less than  $\pm 5 \mu\text{m}$ . For disk-shaped supercapacitor electrodes with a thickness of a few millimeters, the performance variation from this factor is ex-

pected to be insignificant. For electrodes with  $>10 \text{ mm}$  in the critical dimension, additional process optimization would be necessary. For example, dynamic, constant-flux cooling of the cold surface can create a more uniform pore size distribution for thicker samples, e.g., a few centimeters in size along the height.<sup>[34]</sup>

The results presented in this section indicate that the electrical and electrochemical performance of MX-PS supercapacitors can be controlled and enhanced via our fabrication approach by manipulating various features of the MX-PS electrodes. Although we have not made any attempts to optimize the MX-PS supercapacitors, either by using optimal pore size distribution or by maximizing MXene infiltration and reducing restacking, comparing the areal energy and power densities, MX-PS supercapacitors exhibited a strong performance, highlighting the potential of our MX-PS material system.

The work presented here has far-reaching implications for many emerging and future applications. MXene has significant potential for various applications, including batteries, fuel cells, decarbonization systems, and catalytic devices. An essential step toward fully realizing the advantages of MXene is to create a 3D MXene network. The novel approach introduced in this work can create a conductive 3D MXene network by infiltrating MXene nanosheets into porous silica backbones with controlled porosity. This approach results in the 2D MXene nanoflakes to conformally coat the inner surfaces of the backbone's interconnected open pores. This geometry would enable a direct large-area interaction of passing gases with the 2D MXene, which can find significant applications in decarbonization, catalysis, and steelmaking. A dense shell surrounding the freeze-cast samples<sup>[33]</sup> will help prevent gas leakage from side surfaces in such applications. The fabricated MX-PS material also exhibits strong and directional electrical conductivity. In addition, our MX-PS electrodes can be utilized in a range of device configurations (Figure 5d–f), paving the way for their use in integrated electronic systems<sup>[78]</sup> such as high-performance integrated circuits (ICs),<sup>[79]</sup> and electric vehicles.<sup>[80]</sup>

We showed that the porosity, pore orientation, concentration of the MXene dispersion (infiltrant), and the number of infiltration cycles all affect the electrical conductivity of the MX-PS material. Specifically, multiple infiltrations of a higher porosity backbone (60%) with the maximum MXene concentration ( $180 \text{ mg mL}^{-1}$ ) result in the highest electrical conductivity ( $340 \text{ S m}^{-1}$ ) along the primary pore orientation. Our infiltration approach reduces the bulk restacking issue of Ti<sub>3</sub>C<sub>2</sub>T<sub>x</sub> MXene nanomaterials, leading to a more effective utilization of MXenes. Extended storage of MX-PS samples without hermetic conditions decreases the conductivity due to oxidation; however, a steady state ( $\approx 70\%$  of the initial conductivity) is reached after several weeks. We demonstrated an application of MX-PS by constructing symmetric sandwich-type supercapacitor assemblies using MX-PS electrodes. The electrochemical performance of the MX-PS is enhanced due to pseudocapacitance<sup>[9,65]</sup> and more effective use of the available surface area by the MXene coated onto

MX-PS supercapacitor and pouch cell in (f) at a scan rate of  $10 \text{ mV s}^{-1}$ . h) GCD curves of the single MX-PS supercapacitor and pouch cell in (f) at a current density of  $2 \text{ mA cm}^{-2}$ . The Nyquist and Bode plots of the pouch cell in comparison with the single cell is shown in Figure S15 (Supporting Information).

the pore surfaces. The MX-PS supercapacitors exhibited an excellent areal capacitance ( $7.24 \text{ F cm}^{-2}$ ) and a high energy density ( $0.312 \text{ mWh cm}^{-2}$ ) with only a small amount of active mass loading ( $2.43 \text{ mg cm}^{-2}$ ), indicating substantial MXene utilization. Note that the mass loading used to assess utilization is calculated based on the amount of MXene used in (i.e., deposited within) the electrode after the external surfaces of the samples were cleaned (see Table S2 and Figure S9, Supporting Information).

The ability to tailor the porosity distribution of the backbone through the freeze-casting process, the MXene dispersions, and the infiltration process enables controlling the electrical conductivity and electrochemical capacitance of the MX-PS structures. Although we used  $\text{Ti}_3\text{C}_2\text{T}_x$  MXene as the 2D electronic material and silica for the porous backbones, the proposed approach broadly applies to other 2D and nanoscale materials (e.g., other types of MXene, graphene, carbon nanotubes) and other backbone materials (e.g., other ceramics, polymers), enabling assembling 2D nanomaterials in the 3D space. It is noted, however, that unlike MXene, 2D materials, such as reduced-graphene oxide (rGO) and hexagonal boron nitride (hBN), require specific surfactants to obtain stable aqueous dispersions,<sup>[81]</sup> which would require additional process optimization. The MX-PS samples can also be shaped in multiple configurations such as discs (for supercapacitor electrodes, see Figure S16, Supporting Information), elongated cuboids (for electrical conductivity measurements, see Figures S17 and S18a, Supporting Information), and cubes of  $\approx 8\text{--}10 \text{ mm}$  edge length (for infiltration depth assessment, see Figures S5 and S18b, Supporting Information). These geometries were manually cut out of frozen slurry right after solidification using a double-edge razor blade, owing to the butter-like morphology of frozen slurry. Samples with complex geometries can be obtained using computer-assisted techniques, such as micromachining, or via complex mold structures, enabling their use for different applications.

Our approach can induce electrical conductivity in nonconductive materials, such as ceramics and polymers. Furthermore, the porous structure of MX-PS provides the capability to permeate gases or liquids through the structure. Although a formal cost analysis is beyond the scope of this work, further scaling of our fabrication approach can lead to cost-competitive processes compared to the current state-of-the-art supercapacitors.<sup>[82]</sup> For example, a large cold finger, up to a meter square in size, can be used to create thousands of freeze-cast structures shown in Figure 1a, enabling serial/batch production of backbones. Similarly, following an optimization approach will lead to scaled, batch-level MXene synthesis and infiltration.

### 3. Conclusion

This study introduces a new hybrid material system that includes a 3D arrangement of 2D materials on a porous backbone with controlled porosity. Specifically, we demonstrated the assembly of 2D  $\text{Ti}_3\text{C}_2\text{T}_x$  MXene nanomaterials in 3D space on freeze-cast porous silica backbones through a capillary-driven infiltration approach. In addition to facilitating the 3D arrangement of 2D materials, the porous backbone provides mechanical strength, electrical insulation, and gas/liquid permeability, all of which are desirable for electrochemical applications. The

microstructure analysis indicated that the thin-layer morphology of the MXene is conformal to the internal pore surfaces, effectively mitigating restacking of nanoflakes. The experimental results revealed outstanding electrical conductivity that can be finely tuned by controlling the MXene concentration of the infiltrant, the number of infiltration cycles, and the porosity of the backbone. In addition, the selective orientation of the pores enabled anisotropic electrical conductivity of the fabricated MX-PS electrodes. The MXene-infiltrated porous silica electrodes integrated into sandwich-type supercapacitors produced a strong electrochemical performance, demonstrating the exceptional utilization of MXene. The presented approach can widely apply to other 2D and nanoscale materials, such as graphene or carbon nanotubes, and other backbone materials, such as ceramics, metals, or polymers, enabling a broad range of emerging and novel applications that utilize the novel material system introduced in this work.

### 4. Experimental Section

**Freeze Casting of Silica:** The preparation steps of porous silica via freeze casting, as depicted in Figure 1a, were the same as those in the previous work.<sup>[33]</sup> First, an anionic dispersant (Hypermer KD-24, Croda, Inc., Princeton, NJ, USA) was mixed with camphene ( $\text{C}_{10}\text{H}_{16}$ , CAS79-92-5, Sigma-Aldrich, St Louis, MO, USA) on a magnetic hot plate at  $60 \text{ }^\circ\text{C}$  for 30 min. Camphene is a nonpolar solvent when liquid and its melting point is  $46\text{--}52 \text{ }^\circ\text{C}$ . Then, preheated silica powder ( $d_{50} = 400 \text{ nm}$ , US1133M, US Research Nanomaterials, Inc., Houston, TX, USA) was gradually added to this mixture of molten camphene and dispersant while being stirred to ensure uniform coverage of the dispersant on the particle surfaces to avoid agglomeration and settling. The ceramic slurry was then subjected to probe sonication (Q125, Qsonica, Newtown, CT, USA) for 20 min, resulting in a stable and well-mixed colloidal dispersion. The prepared slurry was poured into a cylindrical silicone mold (10 mm wall thickness; Dragon Skin, Smooth-On, Macungie, PA, USA) with a copper insert (plug) blocking the bottom opening of the mold. The mold was placed on top of a cold finger for unidirectional solidification. The temperature of the cold finger was set by a closed-loop thermoelectric temperature control system. It consists of a digitally controlled Peltier module (Custom Thermoelectric, LLC, Bishopville, MD, USA), type-K thermocouples (Adafruit Industries, New York, USA), an Arduino board (Mega, SparkFun Electronics, Niwot, CO, USA), and a custom-made recirculating chiller. The demolded frozen samples were manually sliced into the desired geometries (such as cuboids, cubes, or discs). The morphology of the frozen slurry enabled cutting frozen samples before drying, reducing the process complexity, and preventing pore blockage. Then, samples were placed under a fume hood for 12 h for camphene sublimation. Those green samples were then sintered in a tube furnace (Lindberg/Blue M 1200, Thermo Fisher Scientific, Waltham, MA, USA) in a nitrogen environment at  $1200 \text{ }^\circ\text{C}$  for 3 h to obtain the porous silica parts. The sintering profile included a heating rate of  $5 \text{ }^\circ\text{C min}^{-1}$  to  $800 \text{ }^\circ\text{C}$ , followed by  $1 \text{ }^\circ\text{C min}^{-1}$  to  $1200 \text{ }^\circ\text{C}$ , and a 3 h dwell period at this temperature. The sample was then cooled down to room temperature with a maximum cooling rate of  $5 \text{ }^\circ\text{C min}^{-1}$  to prevent cracks from forming.

The pore morphology characteristics, such as the distributions of equivalent pore size, maximum Feret diameter, and pore orientation of the freeze-cast silica samples are given in Figure S1 (Supporting Information). Note that the cross-sectional dimensions of the rectangular prism samples used in this study are ( $\approx 1 \text{ mm} \times \approx 1 \text{ mm}$ ), which are more than 20 times larger than the average pore size ( $46.3 \text{ }\mu\text{m}$ ) of the freeze-cast silica with 60% porosity. The analysis showed that there are more than 350 pores in each cross-section, providing a statistically significant sample size.

**Preparation of MXene Dispersion:** To prepare the MXene dispersion,  $\text{Ti}_3\text{C}_2\text{T}_x$  MXene flakes were synthesized using the minimally intensive layer

delamination (MILD) method.<sup>[10]</sup> Briefly, Ti<sub>3</sub>AlC<sub>2</sub> MAX powder (<40 μm, Carbon-Ukraine Ltd., Kyiv, Ukraine) was etched with a mixture of hydrochloric acid and lithium fluoride under continuous stirring at room temperature for 24 h. Subsequently, the synthesized acidic Ti<sub>3</sub>C<sub>2</sub>T<sub>x</sub> MXene was washed several times with DI water to increase its pH up to 6. At each wash cycle, MXene was dispersed into the newly added DI water by shaking the container manually, and the obtained slurry was centrifuged to precipitate Ti<sub>3</sub>C<sub>2</sub>T<sub>x</sub> flakes while discarding the liquid part. At the last wash cycle, ≈5 mL DI water was added to the precipitated Ti<sub>3</sub>C<sub>2</sub>T<sub>x</sub> to create a high-concentration mixture. The overall preparation procedure is shown in Figure S19a (Supporting Information). The MXene concentration of the prepared dispersion was calculated using thermogravimetric analysis (TGA). The obtained dispersion was then diluted to the desired concentrations of 45, 90, 135, and 180 mg mL<sup>-1</sup> by adding DI water. A synthesized MXene dispersion is shown in Figure 1c.

**Fabrication of MXene Aerogels:** To obtain the MXene aerogel, the synthesized MXene dispersion was diluted to a specific concentration of 30.45 mg mL<sup>-1</sup>. It is important to note that this value shows the amount of MXene (per volume) distributed in 3D space within silica backbones as a result of the infiltration approach (see Table S2, Supporting Information). The aqueous dispersion with 30.45 mg mL<sup>-1</sup> MXene concentration was then filled into a cylindrical silicone mold with a copper insert at the bottom, the same geometry as the MX-PS samples. To realize unidirectional freezing, the mold was placed on a cold finger placed in liquid nitrogen. The frozen sample was then kept inside a lyophilizer (Harvest Right, UT) for drying. After a 27 h long drying cycle, the cylindrical MXene aerogel was obtained. The cuboid MXene aerogels used for electrical conductivity measurement (Figure S6, Supporting Information) were obtained by placing the MXene dispersion in a trench of 1 mm × 1 mm × 10 mm carved inside a block polydimethylsiloxane (PDMS); followed by a freezing process in liquid nitrogen and drying in the same lyophilizer.

**MXene Characterization:** The size (hydrodynamic diameter) distribution of as-synthesized Ti<sub>3</sub>C<sub>2</sub>T<sub>x</sub> MXene nanoflakes, given in Figure 1d, was determined using the dynamic light scattering technique (Malvern Zetasizer Nano, model Zen 3600, Malvern, UK). Transmission electron microscopy (TEM) and selected-area diffraction (SAED) images were taken using an FEI Tecnai F20 microscope (Hillsboro, OR, USA) at an accelerating voltage of 200 kV. Samples were prepared by drop-casting a Ti<sub>3</sub>C<sub>2</sub>T<sub>x</sub> MXene dispersion on a lacey carbon film of a 200-mesh copper grid. The TEM image of a single Ti<sub>3</sub>C<sub>2</sub>T<sub>x</sub> MXene flake is shown in Figure 1e; and Figure S20 (Supporting Information). Thermogravimetric analysis (TGA Q50, TA Instruments, New Castle, DE, USA) of MXene was performed to determine the concentration of the saturated aqueous MXene dispersions by precisely measuring the change in mass as with the rising temperatures up to 300 °C under nitrogen. As shown in Figure 1f; and Figure S12b (Supporting Information), the measured mass remains constant as the water evaporates during TGA. The remaining (solid) mass value at 200 °C was used as the mass of the MXene in the initial dispersion. Finally, the concentration was calculated by dividing the mass value by the initial slurry volume.

**Preparation of MX-PS:** The sintered porous silica samples were placed inside individual vials. MXene dispersion with a specific concentration (300–400 μL) was added to each vial to submerge the sample fully. To facilitate the infiltration process, the vials were placed in a vacuum. The vacuuming duration was selected as 10 min to avoid excessive evaporation affecting the dispersion's MXene concentration. The vials were then sealed and refrigerated for 12 h to minimize MXene oxidation<sup>[39]</sup> during the wetting of the backbone and accompanying MXene transport into the pores. The images of freeze-cast silica samples in a vial during the vacuum-assisted (capillary) infiltration process are given in Figure S14 (Supporting Information). The infiltration duration of 12 h was determined based on a preliminary study that investigated the effect of infiltration duration on conductivity, as shown in Figure S4d (Supporting Information). The infiltrated samples were then placed in clean vials and dried in a vacuum chamber for 12 h. At the end of the infiltration and drying processes, the dried MXene nanosheets were thinly coated on both the internal and ex-

ternal surfaces of the samples. The accumulated MXene on the external surfaces was carefully cleaned with damp foam-tipped swabs (see Figure S15, Supporting Information) to prevent potential blockage of the pore entrances and to eliminate the effect of this surface layer on the electrical measurements. The obtained MXene-infiltrated porous silica (MX-PS) samples were stored under a vacuum (Rocker 800, Rocker Scientific Co., Ltd, Taiwan) at 4 °C to minimize oxidation until measurements are performed.

**Compression Tests:** For the assessment of the compressive properties of the porous silica samples (cylindrical geometry with ≈10 mm diameter and 10 mm height), a universal testing machine (5969, Instron, Norwood, MA, USA) with a 1 kN load cell was used. The effective elastic modulus of porous silica was much lower than the frame of the test apparatus. As a result, the platen displacement was taken as the displacement of the samples and used for the calculation of their engineering strain. For MXene aerogels (cylindrical geometry with ≈10 mm diameter and 10 mm height), due to the weaker mechanical properties of samples, a dynamic mechanical analyzer (RSA-G2 Solids Analyzer, TA Instruments, New Castle, DE, USA) with a 50 N load cell was used to obtain their compressive behavior. Engineering stress and engineering strain responses of more than four samples were obtained for each sample type.

**Electrical/Electrochemical Measurements—Four-Wire Resistance Measurements and Conductivity Calculations:** Elongated cuboid samples (with ≈1 mm × 1 mm × 10 mm dimensions, see Figures S17 and S18a, Supporting Information) were used to determine electrical conductivity. Longitudinal four-wire resistance measurements were performed using an ohmmeter (34470A, Keysight, Santa Rosa, CA, USA). To minimize contact resistance, a conductive paint (PELCO Conductive Silver Paint, Ted Pella, Inc., Redding, CA, USA) was applied at the sample-wire junctions. The sample dimensions were precisely measured by a wide-area 3D measurement system (VR5200, Keyence Corporation, Osaka, Japan).

**Electrical/Electrochemical Measurements—Supercapacitor Measurements:** All supercapacitor measurements were performed in a symmetric two-electrode sandwich configuration (Figure 4a; and Figure S16, Supporting Information), where the anode and cathode electrodes were made of disc-shaped MX-PS samples with a diameter of ≈10 mm and a thickness of about 1 mm. A porous polypropylene membrane (3501, Celgard LLC, Charlotte, NC, USA) was used as the separator and 3 M poly(vinyl alcohol) (PVA)/H<sub>2</sub>SO<sub>4</sub> was used as the electrolyte. To ensure good electrical conductivity, a thin layer of conductive silver adhesive was applied to the outer surfaces of the MX-PS electrodes as current collectors. Copper tape was attached to these current collectors, and a secondary layer of silver adhesive was thinly coated on the surface, covering the copper tape, to improve the contact region. To prevent oxidation, the copper tape was entirely sealed with Kapton tape, except for the contact region with the electrode. Finally, the prepared electrodes and the separator were sandwiched and packed together with Kapton tape.

Cyclic voltammetry (CV) and GCD tests were performed within the potential range of 0–0.5 V,<sup>[83]</sup> which was selected to avoid parasitic reactions at low rates and oxidation of Ti<sub>3</sub>C<sub>2</sub>T<sub>x</sub> MXene.<sup>[84]</sup> EIS was performed at open circuit potential with an amplitude of 5 mV, from 10 mHz to 10 kHz. The supercapacitor capacitance (C<sub>SC</sub>) was then calculated<sup>[85]</sup> using the cyclic voltammetry (CV) curve as

$$C_{SC} = \frac{\int I(V) dV}{k\Delta V} \quad (1)$$

where  $I$  is the current (A) in the negative CV curve,  $k$  is the scan rate (V s<sup>-1</sup>), and  $\Delta V$  is the operating voltage window (V). The gravimetric and areal specific capacitances of devices were determined by dividing the capacitance by the total mass or projection area of electrodes (i.e., the circular area of the overlapping electrodes), respectively.

The areal energy density ( $E_A$ , mWh cm<sup>-2</sup>) and areal power density ( $P_A$ , mW cm<sup>-2</sup>) of the supercapacitors were calculated using the areal

capacitance of the device ( $C_A$ , F cm<sup>-2</sup>), the operating voltage ( $V$ , V), and the discharge time ( $\Delta t_d$ , s) as

$$E_A = \frac{1000}{2 \times 3600} C_A V^2 \quad (2)$$

and

$$P_A = \frac{3600}{\Delta t_d} E_A \quad (3)$$

**Characterization of Structure and Properties:** To analyze the microstructure of MX-PS samples, a straight scoring mark was made in the middle of the sample, and the sample was broken into two pieces along this mark. This approach was favored over cross-sectioning using a diamond saw to minimize the potential damage to the microstructure (e.g., deep cracks and filling of pores with sawdust). The inner surfaces (cross-sections) created through breakage exhibited some height variations, as shown in Figure 2; and Figure S2a (Supporting Information). The surface microscopy images of the as-produced samples (porous silica and MX-PS electrodes) were captured and analyzed using SEM (Quanta600 FEG, FEI, Hillsboro, OR, USA) and energy-dispersive X-ray spectroscopy (EDX, Oxford Inca, Oxford Instruments, UK). Electrochemical measurements, including EIS, CV, and GCD, of the assembled supercapacitors were recorded by a potentiostat/galvanostat workstation (VersaSTAT3, Princeton Applied Research, Ametek, Inc., Berwyn, PA, USA). All experiments and electrochemical analyses of the prepared supercapacitors were performed in ambient conditions.

## Supporting Information

Supporting Information is available from the Wiley Online Library or from the author.

## Acknowledgements

The authors acknowledge the use of the Materials Characterization Facility at Carnegie Mellon University supported by Grant No. MCF-677785. The authors also wish to thank Dr. Mark Snyder and Mr. Eric Bell of Vesuvius Plc. (Pittsburgh, PA, USA) for their valuable assistance in conducting the mercury porosimetry analyses, and Ph.D. candidate Jonathan Locker from the Islam group at Carnegie Mellon University for his assistance in the characterization of colloidal dispersions. This project was financed in part by funding from the Commonwealth of Pennsylvania, Department of Community and Economic Development.

## Conflict of Interest

The authors declare no conflict of interest.

## Author Contributions

O.B.O. and R.P.P. directed the research. M.A., O.B.O., and R.P.P. designed the experiments. M.A. carried out the experiments. B.Y. helped with MXene synthesis and provided technical inputs on the experiments. M.A. wrote the first draft of the paper. All authors contributed to interpreting the data. M.A., O.B.O., and R.P.P. prepared and edited the manuscript.

## Data Availability Statement

The data that support the findings of this study are available from the corresponding author upon reasonable request.

## Keywords

3D assembly of 2D materials, conductive ceramics, MXenes, porous backbone, supercapacitors

Received: May 19, 2023  
Revised: August 14, 2023  
Published online:

- [1] M. Naguib, M. Kurtoglu, V. Presser, J. Lu, J. Niu, M. Heon, L. Hultman, Y. Gogotsi, M. W. Barsoum, *Adv. Mater.* **2011**, *23*, 4248.
- [2] B. Anasori, M. R. Lukatskaya, Y. Gogotsi, *Nat. Rev. Mater.* **2017**, *2*, 16098.
- [3] X. Xie, Y. Xue, L. Li, S. Chen, Y. Nie, W. Ding, Z. Wei, *Nanoscale* **2014**, *6*, 11035.
- [4] Q. Peng, J. Guo, Q. Zhang, J. Xiang, B. Liu, A. Zhou, R. Liu, Y. Tian, *J. Am. Chem. Soc.* **2014**, *136*, 4113.
- [5] a) X. F. Yu, Y. C. Li, J. B. Cheng, Z. B. Liu, Q. Z. Li, W. Z. Li, X. Yang, B. Xiao, *ACS Appl. Mater. Interfaces* **2015**, *7*, 13707; b) H. Liu, C. Duan, C. Yang, W. Shen, F. Wang, Z. Zhu, *Sens. Actuators, B* **2015**, *218*, 60.
- [6] a) X. Li, Z. Huang, C. E. Shuck, G. Liang, Y. Gogotsi, C. Zhi, *Nat. Rev. Chem.* **2022**, *6*, 389; b) S. Pinilla, J. Coelho, K. Li, J. Liu, V. Nicolosi, *Nat. Rev. Mater.* **2022**, *7*, 717; c) D. Deng, K. Novoselov, Q. Fu, N. Zheng, Z. Tian, X. Bao, *Nat. Nanotechnol.* **2016**, *11*, 218.
- [7] M. R. Lukatskaya, S. Kota, Z. Lin, M.-Q. Zhao, N. Shpigel, M. D. Levi, J. Halim, P.-L. Taberna, M. W. Barsoum, P. Simon, Y. Gogotsi, *Nat. Energy* **2017**, *2*, 17105.
- [8] J. Yan, C. E. Ren, K. Maleski, C. B. Hatter, B. Anasori, P. Urbankowski, A. Sarycheva, Y. Gogotsi, *Adv. Funct. Mater.* **2017**, *27*, 1701264.
- [9] J. Wen, W. Zhang, L. Zhang, X. Zhang, Y.-X. Yu, *Chem. Phys. Lett.* **2021**, *775*, 138666.
- [10] M. Alhabeb, K. Maleski, B. Anasori, P. Lelyukh, L. Clark, S. Sin, Y. Gogotsi, *Chem. Mater.* **2017**, *29*, 7633.
- [11] Q. Wang, S. Wang, X. Guo, L. Ruan, N. Wei, Y. Ma, J. Li, M. Wang, W. Li, W. Zeng, *Adv. Electron. Mater.* **2019**, *5*, 1900537.
- [12] H. Tetik, J. Orangi, G. Yang, K. Zhao, S. B. Mujib, G. Singh, M. Beidaghi, D. Lin, *Adv. Mater.* **2022**, *34*, 2104980.
- [13] J. Orangi, F. Hamade, V. A. Davis, M. Beidaghi, *ACS Nano* **2020**, *14*, 640.
- [14] P. Lin, J. Xie, Y. He, X. Lu, W. Li, J. Fang, S. Yan, L. Zhang, X. Sheng, Y. Chen, *Sol. Energy Mater. Sol. Cells* **2020**, *206*, 110229.
- [15] a) M. Han, X. Yin, K. Hantanasirisakul, X. Li, A. Iqbal, C. B. Hatter, B. Anasori, C. M. Koo, T. Torita, Y. Soda, L. Zhang, L. Cheng, Y. Gogotsi, *Adv. Opt. Mater.* **2019**, *7*, 1900267; b) M.-K. Xu, J. Liu, H.-B. Zhang, Y. Zhang, X. Wu, Z. Deng, Z.-Z. Yu, *Ind. Eng. Chem. Res.* **2021**, *60*, 4342.
- [16] Z. Wu, T. Shang, Y. Deng, Y. Tao, Q. H. Yang, *Adv. Sci.* **2020**, *7*, 1903077.
- [17] Y. Xu, K. Sheng, C. Li, G. Shi, *ACS Nano* **2010**, *4*, 4324.
- [18] S. Zheng, Z. Li, Z. S. Wu, Y. Dong, F. Zhou, S. Wang, Q. Fu, C. Sun, L. Guo, X. Bao, *ACS Nano* **2017**, *11*, 4009.
- [19] L. Chen, L. Guo, Y. Wu, Y. Jia, Z. Li, X. Chen, *RSC Adv.* **2013**, *3*, 13926.
- [20] X. Li, Q. Guan, Z. Zhuang, Y. Zhang, Y. Lin, J. Wang, C. Shen, H. Lin, Y. Wang, L. Zhan, *Ann. Cardiothorac. Surg.* **2023**, *17*, 1653.
- [21] A. Levitt, S. Seyedin, J. Zhang, X. Wang, J. M. Razal, G. Dion, Y. Gogotsi, *Small* **2020**, *16*, 2002158.
- [22] C. Yang, X. Wu, H. Xia, J. Zhou, Y. Wu, R. Yang, G. Zhou, L. Qiu, *ACS Nano* **2022**, *16*, 2699.
- [23] R. Wang, T. Zhang, X. Cheng, J. Xiao, H. Gao, *Ceram. Int.* **2022**, *48*, 20324.
- [24] L. Li, M. Zhang, X. Zhang, Z. Zhang, *J. Power Sources* **2017**, *364*, 234.



- [25] W. Yang, J. Yang, J. J. Byun, F. P. Moissinac, J. Xu, S. J. Haigh, M. Domingos, M. A. Bissett, R. A. W. Dryfe, S. Barg, *Adv. Mater.* **2019**, *31*, 1902725.
- [26] J. Zhou, J. Yu, L. Shi, Z. Wang, H. Liu, B. Yang, C. Li, C. Zhu, J. Xu, *Small* **2018**, *14*, 1803786.
- [27] A. VahidMohammadi, J. Moncada, H. Chen, E. Kayali, J. Orangi, C. A. Carrero, M. Beidaghi, *J. Mater. Chem. A* **2018**, *6*, 22123.
- [28] W. Chen, M. Luo, K. Yang, C. Liu, D. Zhang, X. Zhou, *Chem. Eng. J.* **2021**, *423*, 130242.
- [29] M. Fortunato, I. Bellagamba, A. Tamburrano, M. S. Sarto, *Sensors* **2020**, *20*, 4406.
- [30] Z. Chen, W. Ren, L. Gao, B. Liu, S. Pei, H.-M. Cheng, *Nat. Mater.* **2011**, *10*, 424.
- [31] Z. Pan, C. Yang, Z. Chen, X. Ji, *Nano Res.* **2022**, *15*, 8991.
- [32] A. A. Zakhidov, R. H. Baughman, Z. Iqbal, C. Cui, I. Khayrullin, S. O. Dantas, J. Marti, V. G. Ralchenko, *Science* **1998**, *282*, 897.
- [33] M. Arslanoglu, O. B. Ozdoganlar, R. Panat, *J. Am. Ceram. Soc.* **2022**, *105*, 5114.
- [34] S. Deville, *Freezing Colloids: Observations, Principles, Control, and Use: Applications in Materials Science, Life Science, Earth Science, Food Science, and Engineering*, Springer, Cham, Switzerland **2017**.
- [35] S. Deville, E. Saiz, A. P. Tomsia, *Acta Mater.* **2007**, *55*, 1965.
- [36] S. M. Miller, X. Xiao, K. T. Faber, *J. Eur. Ceram. Soc.* **2015**, *35*, 3595.
- [37] B. Akuzum, K. Maleski, B. Anasori, P. Lelyukh, N. J. Alvarez, E. C. Kumbur, Y. Gogotsi, *ACS Nano* **2018**, *12*, 2685.
- [38] S. Shen, T. Ke, K. Rajavel, K. Yang, D. Lin, *Small* **2020**, *16*, e2002433.
- [39] C. J. Zhang, S. Pinilla, N. McEvoy, C. P. Cullen, B. Anasori, E. Long, S.-H. Park, A. Seral-Ascaso, A. Shmeliov, D. Krishnan, C. Morant, X. Liu, G. S. Duesberg, Y. Gogotsi, V. Nicolosi, *Chem. Mater.* **2017**, *29*, 4848.
- [40] S. B. Nasrallah, P. Perre, *Int. J. Heat Mass Transfer* **1988**, *31*, 957.
- [41] R. K. Lade Jr., K. S. Jochem, C. W. Macosko, L. F. Francis, *Langmuir* **2018**, *34*, 7624.
- [42] E. Rio, A. Daerr, F. Lequeux, L. Limat, *Langmuir* **2006**, *22*, 3186.
- [43] P. J. Yunker, T. Still, M. A. Lohr, A. G. Yodh, *Nature* **2011**, *476*, 308.
- [44] R. D. Deegan, O. Bakajin, T. F. Dupont, G. Huber, S. R. Nagel, T. A. Witten, *Nature* **1997**, *389*, 827.
- [45] H. Hu, R. G. Larson, *J. Phys. Chem. B* **2002**, *106*, 1334.
- [46] B. J. Park, E. M. Furst, *Soft Matter* **2011**, *7*, 7676.
- [47] E. B. Secor, P. L. Prabhuram, K. Puntambekar, M. L. Geier, M. C. Hersam, *J. Phys. Chem. Lett.* **2013**, *4*, 1347.
- [48] Y. Li, S. Huang, C. Wei, D. Zhou, B. Li, C. Wu, V. N. Mochalin, *ACS Appl. Mater. Interfaces* **2021**, *13*, 4682.
- [49] Y. Zhan, B. Nan, Y. Liu, E. Jiao, J. Shi, M. Lu, K. Wu, *Chem. Eng. J.* **2021**, *421*, 129733.
- [50] Y. Li, S. Huang, C. Wei, C. Wu, V. N. Mochalin, *Nat. Commun.* **2019**, *10*, 3014.
- [51] X. Zhao, A. Vashisth, J. W. Blivin, Z. Tan, D. E. Holta, V. Kotasthane, S. A. Shah, T. Habib, S. Liu, J. L. Lutkenhaus, M. Radovic, M. J. Green, *Adv. Mater. Interfaces* **2020**, *7*, 2000845.
- [52] Z. Pan, F. Cao, X. Hu, X. Ji, *J. Mater. Chem. A* **2019**, *7*, 8984.
- [53] B. Chen, Q. Song, Z. Zhou, C. Lu, *Adv. Mater. Interfaces* **2021**, *8*, 2002168.
- [54] Z. Pan, L. Kang, T. Li, M. Waqar, J. Yang, Q. Gu, X. Liu, Z. Kou, Z. Wang, L. Zheng, J. Wang, *ACS Nano* **2021**, *15*, 12975.
- [55] M. L. Braunger, C. A. Escanhoela, I. Fier, L. Walmsley, E. C. Ziemath, *J. Non-Cryst. Solids* **2012**, *358*, 2855.
- [56] A. Fick, *London, Edinburgh, Dublin Philos. Mag. J. Sci.* **1855**, *10*, 30.
- [57] F. Lux, *J. Mater. Sci.* **1993**, *28*, 285.
- [58] W. Eom, H. Shin, R. B. Ambade, S. H. Lee, K. H. Lee, D. J. Kang, T. H. Han, *Nat. Commun.* **2020**, *11*, 2825.
- [59] C. K. Batchelor, G. K. Batchelor, *An Introduction to Fluid Dynamics*, Cambridge University Press, Cambridge, UK **1967**.
- [60] J. Zhang, N. Kong, S. Uzun, A. Levitt, S. Seyedin, P. A. Lynch, S. Qin, M. Han, W. Yang, J. Liu, X. Wang, Y. Gogotsi, J. M. Razal, *Adv. Mater.* **2020**, *32*, 2001093.
- [61] T. S. Mathis, K. Maleski, A. Goad, A. Sarycheva, M. Anayee, A. C. Foucher, K. Hantanasirisakul, C. E. Shuck, E. A. Stach, Y. Gogotsi, *ACS Nano* **2021**, *15*, 6420.
- [62] Y. Chae, S. J. Kim, S. Y. Cho, J. Choi, K. Maleski, B. J. Lee, H. T. Jung, Y. Gogotsi, Y. Lee, C. W. Ahn, *Nanoscale* **2019**, *11*, 8387.
- [63] M. D. Stoller, R. S. Ruoff, *Energy Environ. Sci.* **2010**, *3*, 1294.
- [64] Y. Jiang, J. Liu, *Energy Environ. Mater.* **2019**, *2*, 30.
- [65] N. Kurra, S. Uzun, G. Valourouthu, Y. Gogotsi, *Energy Storage Mater.* **2021**, *39*, 347.
- [66] K. Gholami laelabadi, R. Moradian, I. Manouchehri, *ACS Appl. Energy Mater.* **2021**, *4*, 6697.
- [67] B.-A. Mei, O. Munteshari, J. Lau, B. Dunn, L. Pilon, *J. Phys. Chem. C* **2017**, *122*, 194.
- [68] A. S. Etman, J. Halim, J. Rosen, *Mater. Today Energy* **2021**, *22*, 100878.
- [69] S. Kumar, M. A. Rehman, S. Lee, M. Kim, H. Hong, J.-Y. Park, Y. Seo, *Sci. Rep.* **2021**, *11*, 649.
- [70] K. Maleski, C. E. Ren, M. Q. Zhao, B. Anasori, Y. Gogotsi, *ACS Appl. Mater. Interfaces* **2018**, *10*, 24491.
- [71] X. Zhang, Y. Liu, S. Dong, J. Yang, X. Liu, *J. Alloys Compd.* **2019**, *790*, 517.
- [72] W. Tian, A. VahidMohammadi, M. S. Reid, Z. Wang, L. Ouyang, J. Erlandsson, T. Pettersson, L. Wagberg, M. Beidaghi, M. M. Hamed, *Adv. Mater.* **2019**, *31*, 1902977.
- [73] P. Huang, C. Lethien, S. Pinaud, K. Brousse, R. Laloo, V. Turq, M. Respaud, A. Demortiere, B. Daffos, P.-L. Taberna, *Science* **2016**, *351*, 691.
- [74] M. Ghidui, M. R. Lukatskaya, M. Q. Zhao, Y. Gogotsi, M. W. Barsoum, *Nature* **2014**, *516*, 78.
- [75] M. Luo, D. Zhang, K. Yang, Z. Li, Z. Zhu, S. Xia, H. Y. Yang, W. Chen, X. Zhou, *ACS Appl. Mater. Interfaces* **2022**, *14*, 40460.
- [76] W. Zhao, J. Peng, W. Wang, B. Jin, T. Chen, S. Liu, Q. Zhao, W. Huang, *Small* **2019**, *15*, 1901351.
- [77] K. Zhao, H. Wang, C. Zhu, S. Lin, Z. Xu, X. Zhang, *Electrochim. Acta* **2019**, *308*, 1.
- [78] C. Shen, S. Xu, Y. Xie, M. Sanghadasa, X. Wang, L. Lin, *J. Microelectromech. Syst.* **2017**, *26*, 949.
- [79] a) F. Liu, A. Gutes, I. Laboriante, C. Carraro, R. Maboudian, *Appl. Phys. Lett.* **2011**, *99*, 112104; b) R. Panat, S. Dattaguru, H. Balkan, Y. Min, H. Seh, X. Zhao, *IEEE Trans. Device Mater. Reliab.* **2014**, *14*, 857.
- [80] M. Horn, J. MacLeod, M. Liu, J. Webb, N. Motta, *Econ. Anal. Policy* **2019**, *61*, 93.
- [81] A. F. Khan, D. A. Brownson, C. W. Foster, G. C. Smith, C. E. Banks, *Analyst* **2017**, *142*, 1756.
- [82] H. Dura, J. Perry, T. Lecacou, F. Markoulidis, C. Lei, S. Khalil, M. Decker, M. Weil, in *2013 Int. Conf. on Clean Electrical Power (ICCEP)*, IEEE, Piscataway, NJ, USA **2013**, pp. 516–523.
- [83] a) C. Zhang, L. McKeon, M. P. Kremer, S.-H. Park, O. Ronan, A. Seral-Ascaso, S. Barwich, C. Ó. Coileáin, N. McEvoy, H. C. Nerl, *Nat. Commun.* **2019**, *10*, 1795; b) A. Sangili, B. Unnikrishnan, A. Nain, Y.-J. Hsu, R.-S. Wu, C.-C. Huang, H.-T. Chang, *Energy Storage Mater.* **2022**, *53*, 51.
- [84] A. Inman, T. Hryhorchuk, L. Bi, R. Wang, B. Greenspan, T. Tabb, E. M. Gallo, A. VahidMohammadi, G. Dion, A. Danielescu, Y. Gogotsi, *J. Mater. Chem. A* **2023**, *11*, 3514.
- [85] J. Zhou, X. Wu, Y. Chen, C. Yang, R. Yang, J. Tan, Y. Liu, L. Qiu, H. M. Cheng, *Adv. Funct. Mater.* **2022**, *32*, 2105879.